

Less is More: Efficient Black-box Attribution via Minimal Interpretable Subset Selection

Ruoyu Chen¹, Siyuan Liang¹, Jingzhi Li¹, Shiming Liu, Li Liu¹, *Senior Member, IEEE*, Hua Zhang¹✉, and Xiaochun Cao¹✉, *Senior Member, IEEE*

Abstract—To develop a trustworthy AI system, it is essential to understand its behavior using attribution methods, which aim to identify the input regions that most influence the model's decisions. The primary task of existing attribution methods lies in efficiently and accurately identifying the relationships among input-prediction interactions. Particularly when the input data is discrete, such as images, analyzing the relationship between inputs and outputs poses a significant challenge due to the combinatorial explosion. To solve this issue, we identified a diminishing marginal effect between inputs and outputs, whereby the effectiveness of attribution does not proportionally increase as more inputs are added. In this paper, we propose a novel and efficient black-box attribution mechanism, **LIMA** (Less input is More faithful for Attribution), which reformulates the attribution of important regions as an optimization problem for submodular subset selection. First, to accurately assess interactions, we design a submodular function that quantifies subset importance and effectively captures their impact on decision outcomes. Then, efficiently ranking input sub-regions by their importance for attribution, we improve optimization efficiency through a novel bidirectional greedy search algorithm. **LIMA** identifies both the most and least important samples while ensuring an optimal attribution boundary that minimizes errors. Extensive experiments on eight foundation models (CLIP, ImageBind, LanguageBind, QuiltNet, *etc.*) and six datasets (ImageNet, VGG-Sound, CUB-200-2011, *etc.*) demonstrate that our method provides faithful interpretations with fewer regions and exhibits strong generalization, shows an average improvement of 36.3% in Insertion and 39.6% in Deletion. Additionally, it achieves state-of-the-art attribution faithfulness evaluation metrics (Insertion, Deletion, and average highest confidence) on six datasets. Our method also outperforms the naive greedy search in attribution efficiency, being 1.6 times faster. Furthermore, when explaining the reasons behind model prediction errors, the average highest confidence achieved by our method is, on average, 86.1% higher than that of state-of-the-art attribution algorithms. The code is available at <https://github.com/RuoyuChen10/LIMA>.

Index Terms—Interpretable AI, black-box attribution mechanism, multimodal interpretation, submodular subset selection

1 INTRODUCTION

EXPLAINABLE AI (XAI) techniques have gained significant attention for enabling the transparent and reliable deployment of trustworthy AI systems in real-world applications [1], [2], [3], [4], [5], [6], particularly in high-stakes domains such as healthcare [3] and autonomous driving [7]. The primary objective of XAI is to enhance our understanding of intelligent models, particularly by uncovering the relationships between predictions and input data [8], [9], [10], [11]. To elucidate these associations, attribution-based methods [12], [13], [14], [15] have been developed to interpret the black-box deep neural networks by identifying the contribution of each input feature to the model's predictions. However, attribution methods for black-box AI systems are still an open problem.

Ruoyu Chen, Jingzhi Li, and Hua Zhang (*Corresponding Author*) are with the Institute of Information Engineering, Chinese Academy of Sciences, Beijing 100093, China, and also with the School of Cyber Security, University of Chinese Academy of Sciences, Beijing 100049, China (Email: chenruoyu@iie.ac.cn, lijingzhi@iie.ac.cn, zhanghua@iie.ac.cn).

Siyuan Liang is with the School of Computing, National University of Singapore, 119077, Singapore (Email: pandaliliang521@gmail.com).

Shiming Liu is with the RAMS Lab, Huawei Technologies Co., Ltd., Shenzhen 518129, China (Email: liushiming3@huawei.com).

Li Liu is with the College of Electronic Science and Technology, NUDT, Changsha 430074, China (Email: liuli_nudt@nudt.edu.cn).

Xiaochun Cao (*Corresponding Author*) is with the School of Cyber Science and Technology, Shenzhen Campus of Sun Yat-sen University, Shenzhen 518107, China (Email: caoxiaochun@mail.sysu.edu.cn).

Several advanced attribution methods have been developed, including propagation-based [16], gradient-based [17], [18], [19], [20], Shapley value-based [21], [22], and perturbation-based [9], [23] mechanisms. The primary challenge in achieving perfect fidelity in attribution methods lies in accurately capturing the interactive relationships between inputs and predictions [24], [25]. While existing attribution methods have yielded notable results, they still face several limitations that restrict their applicability in specific scenarios: 1) Computational efficiency, evaluating input-prediction interactions is a combinatorial explosion problem, making it challenging to achieve both efficient and faithful attribution. 2) Inaccurate contribution estimation, many attribution methods use sampling-based approximation strategies to estimate input contributions, which can lead to noisy attribution maps. 3) Region redundancy, when certain subregions are misattributed, either contributing less to, or even negatively affecting, the model's response to the correct category. This issue becomes more pronounced in the case of erroneous predictions.

The core of the attribution problem is to reveal the importance of different regions to the decision outcome and to identify the key regions that have the most significant impact on the final decision. Inspired by submodular subset selection [26], which aims to maximize value by selecting a limited subset, we seek to enhance model interpretability by selecting fewer sub-regions. We identified a diminishing marginal effect between inputs and outputs, whereby the effectiveness of attribution does not proportionally increase as more inputs are added. Motivated by this

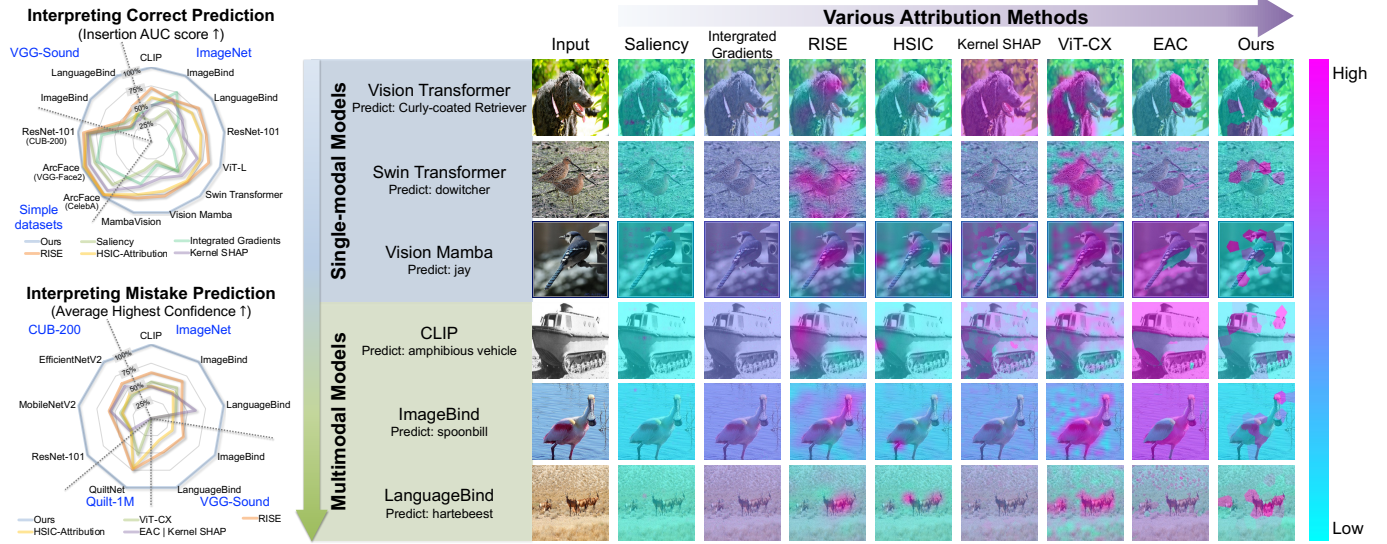


Fig. 1. The left panel illustrates the Insertion and Average Highest Confidence metrics for various attribution mechanisms when attributing the model’s correct and incorrect predictions. Our method shows significant improvements across different datasets and models. The right panel shows the attribution maps of different methods, where our approach avoids noise and unnecessary region redundancy.

approach, the attribution problem can be redefined as a sub-region sorting problem. Specifically, we aim to gradually expand the set of sub-regions, generating an ordered sequence of subsets, thereby systematically addressing the attribution problem. Fig. 1 shows the attribution results of several popular methods across different models and images, highlighting issues such as background noise and region redundancy.

In this paper, we propose **LIMA** (Less input is More faithful for Attribution), a novel and efficient black-box attribution mechanism based on submodular subset selection. We reformulate the attribution problem as a submodular subset selection task to identify the most important regions that influence model decisions, aiming to achieve higher interpretability with fewer, yet more precise, regions. **LIMA** first sparsifies the input into a limited set of fine-grained elements using a semantic or patch-based division method, achieving faithful attribution by iteratively selecting fewer elements. To accurately assess input interactions, a novel submodular function is introduced to quantify the importance of subsets, and we consider four key aspects: semantic consistency, collective effect, the model’s prediction confidence, and the effectiveness of regional semantics. Furthermore, to enhance attribution efficiency, we propose a novel bidirectional greedy search algorithm that simultaneously identifies the most and least important elements.

Extensive experiments on eight foundation models (CLIP [27], ImageBind [28], LanguageBind [29], QuiltNet [30], *etc.*) and six datasets (ImageNet [31], VGG-Sound [32], CUB-200-2011 [33], Celeb-A [34], VGG-Face2 [35], and LC25000 [36]) demonstrate that our method achieves state-of-the-art attribution faithfulness evaluation metrics (Insertion, Deletion, and average highest confidence) with fewer regions and exhibits strong generalization, shows an average improvement of 36.3% in Insertion and 39.6% in Deletion. As shown in the radar chart in Fig. 1, compared to the most advanced attribution methods, our approach shows an average improvement of 36.3% in Insertion. When explaining the reasons behind model prediction errors, the average highest confidence achieved by our method is, on average, 86.1% higher than that of state-of-the-art attribution algorithms. Furthermore, our attribution efficiency is 1.6 times greater than that of the naive greedy search.

Our contributions can be summarized as follows:

- We reformulate the attribution problem as a submodular subset selection problem, aiming to enhance interpretability by identifying a set of smaller, more precise, and fine-grained regions.
- A novel submodular mechanism is introduced to evaluate the importance of subsets, enhancing the fine-grained attribution regions generated by existing algorithms and improving the identification of causes behind image prediction errors. Furthermore, we propose a bidirectional greedy search algorithm that balances attribution efficiency and faithfulness.
- Our analysis shows that as the pre-training scale and model parameters increase, or when models make incorrect predictions, the interaction between input elements becomes more complex, which makes accurate attribution more challenging.
- The proposed method demonstrates strong versatility, enhancing interpretability across various models and datasets. Experimental results indicate that it not only provides high-quality attribution for correctly predicted samples but also effectively identifies the causes of errors in incorrectly predicted samples, particularly for multimodal foundation models.

A preliminary version of this work [8] has been accepted for oral presentation at ICLR 2024. The current version presents several significant advancements over the previous one:

- **Method optimization:** (1) We eliminate the reliance on a prior saliency map by adopting super-pixel segmentation or the Segment Anything approach. This produces semantically richer sub-regions and enhances attribution quality. (2) We introduce a new strategy for assessing the importance scores of ranked sub-regions, which enhances visualization and enables more accurate quantification of their importance. (3) We propose a bidirectional greedy search method to optimize attribution efficiency, which is particularly beneficial for models with a large number of parameters.
- **Analytically:** (4) We observe that as the model’s pre-training scale and the number of parameters increase—or when the model produces incorrect predictions—the interaction between input elements becomes more complex, reducing the effectiveness of traditional attribution methods. (5) We analyze this problem from an interaction perspective and

conclude that our proposed mechanism is better suited for such challenging scenarios. A series of experiments are conducted to validate the effectiveness of our approach.

- **Exhaustive experiments:** (6) We evaluate our attribution approach on models with multiple modalities and architectures, including several multimodal foundation models, as well as ViT and Mamba architectures. The results demonstrate that our approach generalizes well across both multimodal models and various model architectures. (7) We further validate the effectiveness of our approach on multiple datasets, including the large-scale image dataset ImageNet, the medical image dataset LC25000, and the audio dataset VGG-Sound. These results illustrate the versatility of our interpretable attribution method across different data modalities.

The rest of the paper is organized as follows. In Section 2, we review related works. Section 3 provides the preliminaries of submodular theory. In Section 4, we elaborate on our proposed LIMA method, supported by theoretical analysis. Section 5 offers a methodological analysis to highlight the advantages of our approach compared to other mechanisms. The experimental results, along with a visualization analysis, are presented in Section 6, demonstrating the effectiveness of the proposed method. Finally, we conclude the paper in Section 7.

2 RELATED WORK

2.1 Attribution Methods

Inner propagation, activation, and gradient-based methods analyze the internal responses of the network to identify the most important regions of the input. These methods are often referred to as white-box attribution methods because they require access to the model’s internals. Some methods attribute importance by propagating scores back through the layers until reaching the input layer [16]. Other methods rely solely on decision gradients for attribution [37], but these approaches evaluate only the individual effects of pixels or features, without accounting for their collective impact [38]. Some methods combine network activations and gradients for attribution, including Grad-CAM [18], Grad-CAM++ [39], Score-CAM [40], ViT-CX [41], and Grad-ECLIP [20]. However, the effectiveness of these methods depends heavily on the selection of network layers, which significantly influences the quality of interpretation [9]. Moreover, these methods are largely heuristic and lack theoretical guarantees. Path-based methods [17], [19] achieve attribution by selecting a specific integral path. However, this approach is highly sensitive to parameters such as baseline and path choice. Additionally, since the gradient must be integrated, applying this method to large models may be limited by computational resources.

Shapley value estimation-based methods attribute model predictions by estimating the Shapley value [42] of each input region or feature. This is accomplished by calculating the marginal contribution of each region or feature and combining these contributions linearly. However, calculating the Shapley value is an exponential complexity problem. To address this, some model-agnostic methods estimate SHAP values by sampling subsets of features. For example, Kernel SHAP [21] determines feature importance through sampling and the application of specially weighted linear regression. EAC [22] estimates Shapley values by sampling sub-regions defined by the Segment Anything model and using a linear surrogate model. In addition, model-specific methods have been developed to reduce redundant subsets by

leveraging unique model structures. HarsanyiNet [43], for instance, employs a specialized network based on a CNN architecture to accurately estimate Shapley values in a single propagation, though its scalability is limited. Despite these innovations, the exact computation of Shapley values remains generally impractical due to the exponential complexity associated with increasing data dimensions, making it nearly impossible to apply these methods to large models. Additionally, Kumar *et al.* [44] observed that feature importance evaluation methods based on the Shapley value estimation may risk underestimating the importance of relevant features, resulting in all such features being assigned lower importance values.

Perturbation-based methods operate under the assumption that the internal parameters of the model are unknowable. They assess the importance of input regions by perturbing the input and observing the resulting changes in the output. LIME [45] locally approximates the predictions of a black-box model with a linear model, by only slightly perturbing the input. RISE [23] perturbs the model by inputting multiple random masks and weighting the masks to get the final saliency map. HSIC-Attribution method [9] measures the dependence between the input image and the model output through Hilbert Schmidt Independence Criterion (HSIC) based on RISE. Although these methods are highly portable and applicable to various network architectures, their attribution performance is affected by the grid size used for perturbation [9]. If the grid size is too large, the attribution performance may decline, resulting in insufficient granularity in the attribution regions [8].

Search-based methods attribute the importance of different regions by ranking the sub-regions in order. Shitole *et al.* [46] defined minimal sufficient explanation, which involves identifying a limited region whose confidence response to the model is at least 90% of the response of the entire image. They utilized a heuristic beam search to find these regions. However, this method is only effective when the model exhibits a high prediction confidence, and searching for subregions based solely on changes in confidence is often unstable [8]. Chen *et al.* [8] addressed the challenge of searching for high-confidence regions by modeling the image attribution problem as a submodular subset selection problem. However, the performance of this method is influenced by the quality of a prior saliency map.

Multimodal Attribution: Traditional explanation methods mainly focus on single-modal models like DNNs and CNNs, with emerging approaches for multi-modal models. Some studies have investigated attention mechanisms in multimodal ViT models for attributing input or observation influence on outputs [47], but these methods often lack transferability as they rely on access to internal parameters. Darcet *et al.* [48] leveraged attention maps in ViT as guidance and addressed artifacts by incorporating additional tokens. However, attention maps merely reflect intermediate response strengths without explicitly capturing input-output relationships. Zhao *et al.* [20] attributed the CLIP model using gradients and feature maps, achieving better explanation results than self-attention. Gandelsman *et al.* [49] approximated CLIP token attribution via MLP and multi-head attention decomposition, but the results were limited by omitting layer normalization.

In this paper, we propose a novel solution leveraging submodular subset selection. By sparsifying the input, we refine it into more fine-grained regions and identify the most important sub-regions by maximizing the marginal contribution score. This approach yields more robust interpretability results compared to other attribution methods and strong generation across various modality

tasks (natural images, medical images, and audio), especially for samples with complex feature interactions.

2.2 Error Explanation

Identifying and explaining a model’s errors allows us to understand its flaws better and address them more efficiently. Wu *et al.* [50] identified unstable concepts as false attributes and intervened in these concepts to correct model decisions. However, this process requires precise concept annotations, which is cumbersome. Abid *et al.* [51] evaluated the impact of specific concepts on misclassified images using concept activation vectors, thereby explaining model prediction errors from a conceptual perspective. However, concerns remain about whether traditional unimodal models can truly learn explicit concepts and accurately assess their importance [52]. In this paper, our method explains an individual misclassified sample at the input level by directly identifying the specific input region that led to the incorrect prediction. While this may be challenging for humans to understand, it effectively and accurately pinpoints the region where the model was misclassified, offering guidance for future model corrections.

2.3 Submodular Optimization

Submodular optimization [26] has been successfully studied in multiple application scenarios [53], for example, He *et al.* [54] combined submodular subset selection with a loss function and Shapley value to evaluate and select modality importance in multimodal learning. A small number of studies have also applied this theory to explore model interpretability. Catav *et al.* [55] utilized the maximum marginal contribution from all possible subsets to explain the data’s contribution. Elenberg *et al.* [56] frame the interpretability of black-box classifiers as a combinatorial maximization problem, it achieves similar results to LIME and is more efficient. Chen *et al.* [57] propose a learnable network for instance-wise feature selection to explain deep models, but its scalability is limited. Pervez *et al.* [58] proposed a simple subset sampling alternative based on conditional Poisson sampling, which they applied to interpret both image and text recognition tasks. However, these methods only retained the selected important pixels and observed the recognition accuracy [57]. Chhabra *et al.* [59] interpreted the feature space through submodular subset selection to determine which data is helpful to improve model performance. In this paper, we propose an attribution method based on submodular subset selection theory, achieving SOTA performance according to standard attribution metrics. Our method not only identifies the causes behind incorrect model decisions but also demonstrates strong interpretability and error detection across diverse datasets and networks, highlighting its broad applicability.

2.4 Greedy Search

The greedy search algorithm [60], the most commonly used approach, optimizes submodular functions by iterating through unselected examples and calculating the gain in function value from adding each to the selected set. Some accelerated greedy search algorithms have been proposed. Mirzasoleiman *et al.* [61] proposed a stochastic-greedy algorithm, which randomly samples a portion of the unselected examples and performs greedy selection on that subset. Joseph *et al.* [62] partition the samples into equal-sized, non-overlapping sets, perform greedy selection within each, then merge and further select elements. Note that most of

the above acceleration algorithms focus on subset selection rather than the order of samples. Consequently, they are unsuitable for attribution tasks requiring ordered subset search [8]. In this paper, we propose a bidirectional greedy search strategy to reduce the inference costs of attribution large models, which simultaneously identifies both the most and least important samples. During the greedy search for critical samples, it generates candidates for the least important ones using a submodular function, then selects the least important sample from these candidates. By combining the ordered sets of both critical and non-critical samples, our method produces a more accurate ordered subset with minimal computational overhead.

3 PRELIMINARIES

In this section, we first establish some definitions. Considering a finite set V , given a set function $\mathcal{F} : 2^V \rightarrow \mathbb{R}$ that maps any subset $S \subseteq V$ to a real value. When \mathcal{F} is a submodular function, its definition is as follows:

Definition 1 (Submodular function [63]). *For any set $S_a \subseteq S_b \subseteq V$. Given an element α , where $\alpha \in V \setminus S_b$. The set function \mathcal{F} is a submodular function when it satisfies monotonically non-decreasing ($\mathcal{F}(S_b \cup \{\alpha\}) - \mathcal{F}(S_b) \geq 0$) and:*

$$\mathcal{F}(S_a \cup \{\alpha\}) - \mathcal{F}(S_a) \geq \mathcal{F}(S_b \cup \{\alpha\}) - \mathcal{F}(S_b). \quad (1)$$

Problem formulation: We divide an input data \mathbf{I} into a finite number of sub-regions with a division algorithm $\text{Div}(\cdot)$, denoted as $V = \text{Div}(\mathbf{I}) = \{\mathbf{I}_1^M, \mathbf{I}_2^M, \dots, \mathbf{I}_m^M\}$, where M indicates a sub-region \mathbf{I}^M formed by masking part of \mathbf{I} . Giving a monotonically non-decreasing submodular function $\mathcal{F} : 2^V \rightarrow \mathbb{R}$, the attribution problem can be viewed as maximizing the value $\mathcal{F}(S)$ with limited regions. Mathematically, the goal is to select an ordered set S consisting of a limited number k of sub-regions in the set V that maximize the submodular function \mathcal{F} :

$$\max_{S \subseteq V, |S| \leq k} \mathcal{F}(S), \quad (2)$$

we can transform the attribution problem into a subset selection problem, where the submodular function \mathcal{F} relates design to interpretability. However, solving Eq. 2 is typically an \mathcal{NP} -hard problem. Nemhauser *et al.* [60] proved that a greedy algorithm can produce a subset of values with optimality guarantees in polynomial time. Thus, a greedy search algorithm can be used to maximize the submodular function, thereby explaining the importance ranking of input subregions in the attribution task, and it runs in time $\mathcal{O}(k|V|)$. The total number of samples required for inference is given by $k|V| - \frac{1}{2}k(k-1)$. Typically, we need to sort all subregions, which results in a total number of inferences given by $\frac{1}{2}|V|^2 + \frac{1}{2}|V|$ and the algorithm runs in time $\mathcal{O}(|V|^2)$. The optimality bound of the solution S is given by $\mathcal{F}(S) \geq (1 - 1/e)\mathcal{F}(S^*)$, where S^* denotes the optimal solution and e is the base of the natural logarithm.

4 PROPOSED METHOD

In this section, we introduce a novel method for image attribution based on submodular subset selection theory. Section 4.1 provides a detailed explanation of the sub-region division process. In Section 4.2, we present our custom-designed submodular function. Section 4.3 outlines the attribution algorithm, which utilizes a bidirectional greedy search approach, while Section 4.4 describes the procedure for assigning importance scores to the ordered set. Fig. 2 illustrates the overall framework of our approach.

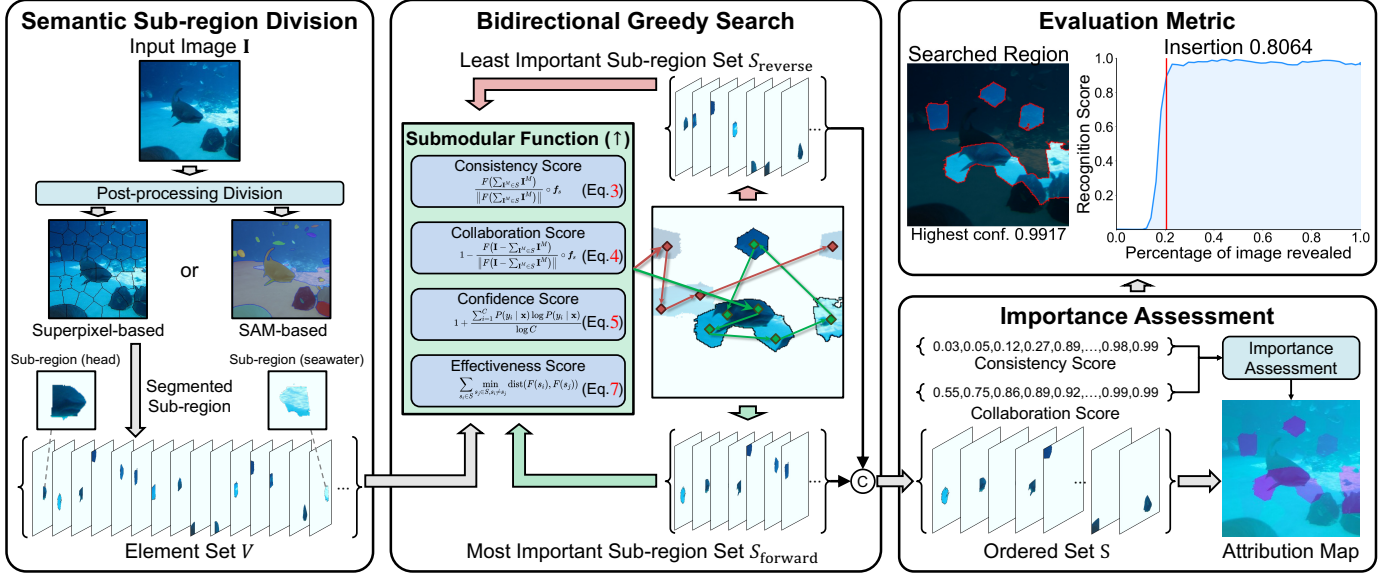


Fig. 2. The framework of the proposed **LIMA** method. We begin by performing semantic sub-region division on the image, either using superpixel-based methods or the Segment Anything algorithm. Next, we apply a bidirectional greedy search algorithm along with a designed submodular function to simultaneously identify the most and least important samples, ranking these sub-regions accordingly. Finally, based on sub-region rankings, we concatenate the most important sample set with the least important sample set and evaluate the importance of each sub-region using consistency and collaboration scores, resulting in enhanced regional visualization. Through the faithfulness metric, our method identifies few regional representations sufficient to activate the model response.

4.1 Sub-region Division

To obtain the interpretable region in an image, we partition the image $\mathbf{I} \in \mathbb{R}^{w \times h \times 3}$ into m sub-regions \mathbf{I}^M with a division algorithm $\text{Div}(\cdot)$, where M indicates a sub-region \mathbf{I}^M formed by masking part of image \mathbf{I} . The division algorithm determines the quality of the search space, thereby influencing the effectiveness of the attribution [8]. Our recommended division strategies $\text{Div}(\cdot)$ are as follows:

- **Superpixel-based division** involves clustering pixels with similar characteristics. For image modality, methods like SLIC [64] can be employed to perform this division, thereby improving attribution efficiency.
- **Semantic-based division** can more effectively distinguish between different concepts and enhance human understanding. Segment Anything (SAM) [65] can be used for zero-shot division. However, since the regions segmented by SAM may overlap, we propose a SAM-based division method. Details can be found in Section D, Algorithm 2 in the supplementary material.
- **Patch-based division** has been studied in traditional methods [23], [66], which can divide the input into regular patch regions.

We can select the appropriate division method for attribution based on the specific input modality.

4.2 Submodular Function Design

In this section, we construct a submodular function to evaluate the order of importance of interpretable regions. To enhance the attribution effect across all samples, we impose four distinct constraints on the selection of sub-regions: consistency, collaboration scores, confidence, and effectiveness. These constraints are used to assess the importance of various subsets.

Consistency Score: We aim to make the representation of the identified image region consistent with the original semantics. Given a target semantic feature or mapping function, \mathbf{f}_s , we make

the semantic features of the searched image region close to the target semantic features. We introduce the consistency score:

$$s_{\text{cons.}}(S, \mathbf{f}_s) = \frac{F(\sum_{\mathbf{I}^M \in S} \mathbf{I}^M)}{\|F(\sum_{\mathbf{I}^M \in S} \mathbf{I}^M)\|} \circ \mathbf{f}_s, \quad (3)$$

where $F(\cdot)$ denotes a pre-trained feature extractor. The target semantic feature \mathbf{f}_s , can either adopt the features computed from the original image using the pre-trained feature extractor, expressed as $\mathbf{f}_s = F(\mathbf{I})$, or directly implement the fully connected layer of the classifier for a specified class. By incorporating the $s_{\text{cons.}}$, our method targets regions that reinforce the desired semantic response. This approach ensures a precise selection that aligns closely with our specific semantic goals.

Collaboration Score: Some individual elements may lack significant individual effects in isolation, but when placed within the context of a group or system, they exhibit an indispensable collective effect. Therefore, we introduce the collaboration score, which is defined as:

$$s_{\text{colla.}}(S, \mathbf{I}, \mathbf{f}_s) = 1 - \frac{F(\mathbf{I} - \sum_{\mathbf{I}^M \in S} \mathbf{I}^M)}{\|F(\mathbf{I} - \sum_{\mathbf{I}^M \in S} \mathbf{I}^M)\|} \circ \mathbf{f}_s, \quad (4)$$

where $F(\cdot)$ denotes a pre-trained feature extractor, \mathbf{f}_s is the target semantic feature. By introducing the collaboration score, we can judge the collective effect of the element. By incorporating the $s_{\text{colla.}}$, our method pinpoints regions whose exclusion markedly affects the model's predictive confidence. This effect underscores the pivotal role of these regions, indicative of a significant collective impact. Such a metric is particularly valuable in the initial stages of the search, highlighting regions essential for sustaining the model's accuracy and reliability.

Confidence Score: The model's confidence in its own predictions is also closely related to interpretability [67] and the entropy of the model output is a key indicator for measuring the uncertainty of the model's predictions [68], [69]. Therefore, we use the entropy of the network output to calculate the confidence score. In the inference, the predictive uncertainty can be calculated as $u = -\frac{\sum_{i=1}^C P(y_i|\mathbf{x}) \log P(y_i|\mathbf{x})}{\log C}$, where $u \in [0, 1]$, $P(y_i|\mathbf{x})$ is

the probability of a specific class output, C is the total number of classes. Thus, the confidence score of the sample \mathbf{x} predicted by the network can be expressed as:

$$s_{\text{conf.}}(\mathbf{x}) = 1 - u = 1 + \frac{\sum_{i=1}^C P(y_i | \mathbf{x}) \log P(y_i | \mathbf{x})}{\log C}. \quad (5)$$

By incorporating the $s_{\text{conf.}}$, we can ensure that the selected regions align closely with the In-Distribution (InD). This score acts as a reliable metric to distinguish regions from out-of-distribution, ensuring alignment with the InD.

Effectiveness Score: Adding different sub-regions may exhibit OR interactions, meaning they have similar marginal contribution scores [24]. We expect to maximize the response of valuable information with fewer regions since some image regions have the same semantic representation. Given an element α , and a sub-set S , we measure the distance between the element α and all elements in the set, and calculate the smallest distance, as the effectiveness score of the judgment element α for the sub-set S :

$$s_e(\alpha | S) = \min_{s_i \in S} \text{dist}(F(\alpha), F(s_i)), \quad (6)$$

where $\text{dist}(\cdot, \cdot)$ denotes the equation to calculate the distance between two elements. Traditional distance measurement methods [70], [71] are tailored to maximize the decision margins between classes during model training, involving operations like feature scaling and increasing angle margins. In contrast, our method focuses solely on calculating the relative distance between features, for which we utilize the general cosine distance. $F(\cdot)$ denotes a pre-trained feature extractor. To calculate the element effectiveness score of a set, we can compute the sum of the effectiveness scores for each element:

$$s_{\text{eff.}}(S) = \sum_{s_i \in S} \min_{s_j \in S, s_i \neq s_j} \text{dist}(F(s_i), F(s_j)). \quad (7)$$

By maximizing the $s_{\text{eff.}}$, we aim to limit the selection of regions with similar semantic representations, thereby increasing the diversity and improving the overall quality of region selection.

Submodular Function: We construct our objective function for selecting elements through a combination of the above scores, $\mathcal{F}(S)$, as follows:

$$\begin{aligned} \mathcal{F}(S) = & \lambda_1 s_{\text{cons.}}(S, \mathbf{f}_s) + \lambda_2 s_{\text{colla.}}(S, \mathbf{I}, \mathbf{f}_s) \\ & + \lambda_3 s_{\text{conf.}}\left(\sum_{\mathbf{I}^M \in S} \mathbf{I}^M\right) + \lambda_4 s_{\text{eff.}}(S), \end{aligned} \quad (8)$$

where $\lambda_1, \lambda_2, \lambda_3$, and λ_4 represent the weighting factors used to balance each score. According to the importance and experience of the scores, we set these parameters to $\lambda_1 = 20$, $\lambda_2 = 5$, $\lambda_3 = 0.05$, and $\lambda_4 = 0.01$ respectively.

Lemma 1 (Diminishing returns). *Consider two sub-sets S_a and S_b in set V , where $S_a \subseteq S_b \subseteq V$. Given an element α , where $\alpha \in V \setminus S_b$. Assuming that α is contributing to model interpretation, then, the function $\mathcal{F}(\cdot)$ in Eq. 8 is a submodular function and satisfies Eq. 1.*

Proof. Please see *suppl. material A.1* for the proof. \square

Lemma 2 (Monotonically non-decreasing). *Consider a subset S , given an element α , assuming that α is contributing to model interpretation. The function $\mathcal{F}(\cdot)$ of Eq. 8 is monotonically non-decreasing.*

Proof. Please see *suppl. material A.2* for the proof. \square

Based on Lemma 1 and Lemma 2, we can prove that the function $\mathcal{F}(\cdot)$ is submodular.

Remark 1. *The quality of the α in the sub-region division influences the search space, thereby affecting the optimization of the submodular function. Higher-quality sub-region division leads to improved attribution performance.*

4.3 Bidirectional Greedy Search Algorithm

Given a set $V = \{\mathbf{I}_1^M, \mathbf{I}_2^M, \dots, \mathbf{I}_m^M\}$, we can follow Eq. 2 to search the interpretable region by selecting k elements that maximize the value of the submodular function $\mathcal{F}(\cdot)$. The above problem can be effectively addressed by implementing a greedy search algorithm. Referring to related works [61], [72], we can use a greedy search to optimize the value of the submodular function. However, greedy search requires traversing all elements in $V \setminus S$, and the computational cost for large models remains high, which reduces the attribution speed. Since attribution typically requires ranking the importance of all features, acceleration methods based on random sampling [61] are not suitable. Sampling-based methods risk missing the most important features, which is critical in the context of attribution.

We propose a bidirectional greedy search algorithm that simultaneously identifies the most important and least important samples, as illustrated in Algorithm 1. Specifically, we utilize two sets: S_{forward} is used to incrementally add the most important elements, while S_{reverse} gradually accumulates the least important elements. As S_{forward} gradually adds the most important elements, it must traverse and evaluate all samples in $V \setminus (S_{\text{forward}} \cup S_{\text{reverse}})$, selecting the one that yields the greatest marginal gain. We simultaneously select n_p candidates for the least important elements based on their marginal gains, denoted as S_p , as we believe that minimal or insignificant gains may indicate the least important elements. S_{reverse} only selects an element from S_p to minimize the submodular value:

$$\min_{\alpha \in S_p} \mathcal{F}(\{\alpha\} \cup S_{\text{reverse}}), \quad (9)$$

note that minimizing the value of \mathcal{F} also satisfies submodularity [26], and its optimal boundary is related to the value of n_p . Although the Algorithm 1 still runs in time $\mathcal{O}(|N|^2)$, compared to the naive greedy search, the total number of elements required for inference is $\frac{1}{4}|N|^2 + \frac{1}{2}|N|n_p - \frac{1}{2}n_p^2 + \frac{1}{2}n_p$, and when n_p is 1, the number of inferences can be reduced by at most $\frac{1}{4}|N|^2$ times. The following theorem demonstrates the optimality bound of the output generated by Algorithm 1.

Theorem 1 (Bidirectional greedy search optimality bound). *Let S denote the solution obtained by the proposed bidirectional greedy search approach from the set V , and let S^* represent the optimal solution. When $\mathcal{F}(\cdot)$ is a submodular function, the solution S satisfies the following approximation guarantee:*

$$\mathcal{F}(S) \geq \left(1 - \frac{1}{e} - \epsilon\right) \mathcal{F}(S^*), \quad (10)$$

where e represents the base of the natural logarithm, and $1 - \epsilon$ is the probability that S_d overlaps with S^* . As n_p increases, ϵ decreases.

Proof. Please see *suppl. material A.3* for the proof. \square

Algorithm 1: The proposed bidirectional greedy search algorithm for interpretable region discovery

Input: Image $\mathbf{I} \in \mathbb{R}^{w \times h \times 3}$, a division algorithm $\text{Div}(\cdot)$, number of pending negative samples n_p .

Output: An ordered set S , where $|S| = |V|$.

```

1  $V \leftarrow \text{Div}(\mathbf{I});$  /* Sub-region division */
2  $k = \frac{1}{2}|V| + \frac{1}{2}n_p;$ 
3  $S \leftarrow \emptyset;$  /* Initiate the operation of submodular subset selection */
4  $S_{\text{forward}} \leftarrow \emptyset;$ 
5  $S_{\text{reverse}} \leftarrow \emptyset;$ 
6 for  $i = 1$  to  $k$  do
7    $S_d \leftarrow V \setminus (S_{\text{forward}} \cup S_{\text{reverse}});$ 
8   if  $S_d == \emptyset$  then
9     break
10   $\alpha \leftarrow \arg \max_{\alpha \in S_d} \mathcal{F}(S_{\text{forward}} \cup \{\alpha\});$  /* Optimize the submodular value */
11   $S_{\text{forward}} \leftarrow S_{\text{forward}} \cup \{\alpha\};$  /* Ascending */
12   $S_d \leftarrow S_d \setminus \alpha;$ 
13  if  $|S_d| > n_p$  then
14     $S_p \leftarrow \text{TOPK}_{\alpha \in S_d}^{\min}(\mathcal{F}(S_{\text{forward}} \cup \{\alpha\}), n_p) \setminus S_{\text{forward}};$ 
15     $\alpha \leftarrow \arg \min_{\alpha \in S_p} \mathcal{F}(\{\alpha\} \cup S_{\text{reverse}});$ 
16     $S_{\text{reverse}} \leftarrow \{\alpha\} \cup S_{\text{reverse}};$  /* Descending */
17 end
18  $S \leftarrow S_{\text{forward}} \cup S_{\text{reverse}};$ 
19 return  $S$ 

```

According to Theorem 1, our method can maintain a good optimality bound even when the model reduces a significant number of sample inferences. This is particularly beneficial for lowering the computational cost of interpreting large models.

4.4 Sub-region Importance Assessment

Although the sub-regions are ranked by importance, the ranking does not consider the degree of difference between them. The importance differences between adjacent sub-regions are unlikely to be uniform. To address this, we propose a simple first-order assignment method based on marginal contribution scores. Equations 3 and 4 are closely related to the model’s decision-making process, allowing us to quantify the marginal effects by analyzing their variations to capture the differences between elements. The attribution score a_i for each element s_i in S is given by:

$$a_i = \begin{cases} b_{\text{base}} & \text{if } i = 1, \\ a_{i-1} - |(s_{\text{cons.}}(S_{[i]}) + s_{\text{colla.}}(S_{[i]})) - (s_{\text{cons.}}(S_{[i-1]}) + s_{\text{colla.}}(S_{[i-1]}))| & \text{if } i > 1, \end{cases} \quad (11)$$

where b_{base} denotes a baseline value, and $S_{[i]}$ represents the set containing the top i elements in the set S . When a new element is added, if the marginal effect does not increase significantly, it suggests that the importance of this element is comparable to that of the previous one. If the marginal effect is negative—indicating that the remaining elements have a counterproductive effect on the model’s decision—the negative impact of the element can be evaluated based on the absolute value of the marginal effect. By assessing the importance of all elements in this manner, we can better visualize which regions are most important and distinguish the differences in importance across sub-regions, enhancing human understandability.

5 METHOD ANALYSIS

In this section, we evaluate the effectiveness of our approach, identify the scenarios in which it is most applicable, and compare it against other baseline attribution algorithms.

Interaction Effect Analysis: Deng *et al.* [10] decompose attribution methods into a weighted combination of independent and interaction effects, which means an individual effect implies that the attribution score for a given pixel is independent of other pixels, whereas an interaction effect indicates that the model predicted score is influenced by multiple other pixels. Drawing inspiration from them, we further analyze our method in terms of the independent and interactive effects of sub-regions. Therefore, let $G(S) = F(S) / \|F(S)\| \circ \mathbf{f}_s$, Eq. 11 for attribution can be restated as follows:

$$\begin{aligned} a_{i+1} &= a_i - \left| G(S_{[i]}) + \nabla G(S_{[i]}) \cdot \alpha - G(S_{[i]}) \right. \\ &\quad \left. + G(S_{[\bar{i}]} - \left(G(S_{[\bar{i}]} - \nabla G(S_{[\bar{i}]} - \alpha) \right) \right| \quad (12) \\ &= a_i - \left| \nabla G(S_{[i]}) \cdot \alpha + \nabla G(S_{[\bar{i}]} - \alpha) \right|, \end{aligned}$$

where $S_{[i]}$ represents the set containing the top i elements in the set S , and its complementary subset is $S_{[\bar{i}]}$, and $\alpha = S_{[i+1]} \setminus S_{[i]}$. From Eq. 12, it is evident that our method represents a simple first-order attribution. By dividing the sub-regions to create a sparse input, a more efficient explanation is obtained. In addition, we observe that, apart from the most important sub-region using the baseline value b_{base} , each sub-region attribution score a_i represents the interaction of all other sub-regions, excluding itself. This indicates that our attribution method accounts for the interaction effects with all sub-regions, rather than merely capturing individual effects. Since our method is based on submodular subset selection, the identified subset $S_{[i]}$ is optimally ensured by searching for the highest marginal contribution within the current subset, thereby identifying the next most important sub-region α along with its actual contribution.

Mainstream Attribution Analysis: Gradients primarily capture individual effects [10], meaning that both propagation-based and gradient-based attribution methods are influenced by these effects to varying extents. The sampling-based Shapley value estimation method and the perturbation-based method also compute attribution scores that account for interaction effects. Kumar *et al.* [44] observed that Shapley value estimation may risk underestimating the importance of relevant features, furthermore, if the interaction of subsets is complex and irregular, it will also affect the accurate estimation of Shapley value. The perturbation-based method assumes that all elements within each sampling subset contribute equally, which may lead to an overestimation of the contribution of certain sub-regions. Chen *et al.* [24] proves that there exists the feature interaction response in the network output, rather than a simple individual response. Based on the above analysis, we posit that our method is particularly advantageous in scenarios with complex feature interactions in model decision-making. Next, we will examine the scenarios under which such complex interactive responses are most likely to arise.

Complex Interaction Situation Analysis: We aim to explore the conditions under which input interactions become more complex. An intuitive approach is to consider the minimum number of input elements required to trigger the activation of the target category response. We define a strong interactive response as a change in the model’s response of more than 0.5 when a new element is added to a subset. To investigate when these strong interactive responses occur, we conducted two experiments: (i) We applied our method to attribute 1000 samples correctly predicted by three different models. We analyzed the insertion curve of each sample and recorded the number of responses where the absolute

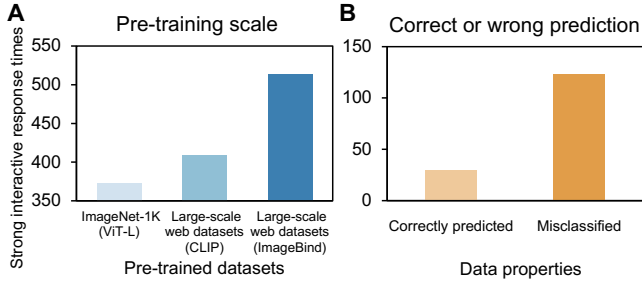


Fig. 3. Statistics of strong interactive response times. **A.** Impact of pre-training scale and model size. **B.** Impact of whether the model correctly predicts.

value of the change exceeded 0.5. As shown in Fig. 3A, models with ViT-L architectures pre-trained on large-scale web datasets exhibit more complex interaction effects than those pre-trained on ImageNet-1K. For larger models, such as ImageBind, the number of complex interactive responses increases significantly. (ii) We also applied our method to 1000 correctly predicted samples and 1000 misclassified samples by ImageBind, analyzing their insertion curves and counting the number of responses with a decrease greater than 0.5. As shown in Fig. 3B, strong interactive responses are more likely to occur in misclassified samples, contributing to prediction errors. Blocking these elements can correct the model’s prediction results. Based on these observations, we have the following hypothesis:

Hypothesis 1. *When the model is pre-trained on a larger dataset, resulting in a larger model size and more complex feature interaction responses during decision-making, our method demonstrates stronger attribution performance compared to baseline attribution methods, especially in cases of sample prediction errors.*

In order to verify the proposed hypothesis, we will conduct a series of experiments in the following section to observe the impact of different model sizes and feature interaction complexities on attribution performance.

6 EXPERIMENTS

In this section, we provide a validation of our **LIMA** mechanism. We begin by describing the datasets and experimental setup in Section 6.1, followed by a detailed explanation of the evaluation metrics in Section 6.2. In Section 6.3, we present the interpretation results of LIMA across multimodal and unimodal models, as well as various network architectures. Section 6.4 demonstrates how LIMA explains the factors influencing model predictions across different modalities and network architectures. Finally, Section 6.5 verifies the effectiveness of each module in the proposed method through a series of ablation experiments.

6.1 Experimental Setup

Datasets. We evaluate the proposed **LIMA** on six datasets: a large-scale natural image dataset, ImageNet [31]; a fine-grained bird dataset, CUB-200-2011 [33]; two face datasets, Celeb-A [34] and VGG-Face2 [35]; a medical image dataset, LC25000 (Lung) [36]; and an audio dataset, VGG-Sound [32].

For the ImageNet dataset, which comprises 1,000 categories, we select five correctly predicted samples from each class in the validation set, resulting in 5,000 images per model to assess image attribution performance. Additionally, two incorrectly predicted samples per class are chosen, yielding a total of 2,000 images per

model, to evaluate our method’s ability to identify the causes of prediction errors.

For the CUB-200-2011 dataset, which consists of 200 bird species, we select three correctly predicted samples from each class in the validation set, totaling 600 images, to evaluate image attribution performance. Additionally, two incorrectly predicted samples per class are chosen, resulting in 400 images, to assess our method’s ability to identify the causes of model prediction errors.

The Celeb-A dataset includes 10,177 identities, from which we randomly select 2,000 identities from the validation set, using one test face image per identity to evaluate our method. Similarly, for the VGG-Face2 dataset, which contains 8,631 identities, we randomly select 2,000 identities from the validation set, with one test face image per identity used for evaluation.

For the LC25000 (Lung) dataset, which includes three lung cell classes, we selected 1,000 misclassified images to assess our method’s effectiveness in attributing errors in medical images.

For the VGG-Sound dataset, containing 309 audio classes, we randomly select two correctly predicted samples from each class in the validation set to assess attribution effectiveness, and one misclassified sample per class to evaluate error attribution.

Implementation Details. We primarily apply **LIMA** to interpret architectures based on CNN, ViT, and Mamba. For the ImageNet dataset, we evaluated our method on four multi-modal foundation models: CLIP (ViT-L) [27], CLIP (ResNet-101), ImageBind (Huge) [28], and LanguageBind (Large) [29], as well as five single-modal pre-trained models: ResNet-101 [73], ViT-Large [74], Swin Transformer (Large) [75], Vision Mamba (Base) [76], and MambaVision (L2) [77]. All models utilized their official pre-trained parameters. For image classification, we used the video encoder of LanguageBind, while for the other models, we employed their respective image encoders. For the face datasets, we evaluated recognition models trained with the ResNet-101 architecture [73] and the ArcFace loss function [71], with an input size of 112×112 pixels. For the CUB-200-2011 dataset, we tested three recognition models built on the ResNet-101, MobileNetV2 [78], and EfficientV2-M [79] architectures. In the case of the LC25000 (Lung) dataset, we employed QuiltNet (ViT/B-32) [30], a vision-language medical foundation model trained on the Quilt-1M dataset. Finally, for the VGG-Sound dataset, we evaluated our method using two foundation models: ImageBind (Huge) and LanguageBind (Large).

For the target semantic feature f_s , in the multimodal foundation model, we utilize the semantic vector encoded by the text encoder. In contrast, for the single-modal model, we directly use the fully connected layer following the backbone. Unless otherwise specified, the number of sub-regions segmented using the SLICO [64] algorithm is fixed at $|V| = 49$, whereas the number of sub-regions generated by the SAM [65] algorithm is not controllable. Our experiments were conducted using the Xplique repository¹, which provides baseline methods and evaluation tools. All experiments were performed on an NVIDIA 4090 GPU.

6.2 Evaluation Metrics

Since attribution methods aim to identify which inputs influenced a model’s decision, the resulting explanations should be evaluated not by humans but by objective faithfulness metrics. We employ four fidelity metrics to evaluate our attribution methods.

1. Xplique: <https://github.com/deel-ai/xplique>

The first is the **Deletion AUC score** [23], which quantifies the reduction in the model’s output when important regions are replaced with a baseline value. A sharp decline in performance indicates that the explanation method effectively identifies the key variables influencing the decision. Let $\mathbf{x}_{[x_T=x_0]}$ denote the input where the T most important variables, according to the attribution map, are set to the baseline value $x_0 = 0$. Given a set $\mathcal{T} = \{T_0, T_1, \dots, T_n\}$, where $T_0 = 0$ and T_n is the input size of \mathbf{x} , this set represents the selected numbers of the most important regions. Then, the Deletion AUC score is given by:

$$\text{Del.} = \sum_{i=1}^n \frac{(f(\mathbf{x}_{[x_{T_i}=x_0]}) + f(\mathbf{x}_{[x_{T_{i-1}}=x_0]})) \cdot (T_i - T_{i-1})}{2T_n}, \quad (13)$$

the lower this metric, the better the attribution performance.

The second metric is the **Insertion AUC score** [23], which quantifies the increase in the model’s output as important regions are progressively revealed. This metric is defined as follows:

$$\text{Ins.} = \sum_{i=1}^n \frac{(f(\mathbf{x}_{[x_{T_i}=x_0]}) + f(\mathbf{x}_{[x_{T_{i-1}}=x_0]})) \cdot (T_i - T_{i-1})}{2T_n}, \quad (14)$$

where $\mathbf{x}_{[x_{\bar{T}}=x_0]}$ denotes the input where elements not belonging to the set \bar{T} are set to the baseline value $x_0 = 0$. The higher this metric, the better the attribution performance.

The third metric is the **average highest confidence** [8], which measures the model’s highest response within a constrained search region. This metric is used to evaluate attribution results for samples that the model incorrectly predicts, assessing whether the method can identify the factors contributing to the model’s incorrect predictions. It is defined as follows:

$$\text{highest conf.} = \max_{T \in \mathcal{T}_{[k]}} (f(\mathbf{x}_{[x_T=x_0]})), \quad (15)$$

where $\mathcal{T}_{[k]}$ denotes the set of most important regions that can be searched, constrained by a search region that does not exceed k . The higher this metric, the better the attribution performance.

The final metric is μ **Fidelity** [80], which measures the correlation between the reduction in the model’s score when variables are set to a baseline state and the importance of those variables. However, since the network’s output is not necessarily a linear combination of its inputs, this metric may not fully capture the quality of the attribution. Nonetheless, it is primarily used to evaluate how effectively our method identifies the importance of sub-regions.

6.3 Faithfulness Analysis

To demonstrate the superiority of our method, we assess its faithfulness, which measures the alignment between the generated explanations and the deep model’s decision-making process [81]. We employ Deletion and Insertion AUC scores, along with μ Fidelity, as evaluation metrics. Our method is evaluated on correctly predicted samples across various modalities and architectures.

6.3.1 Faithfulness on Multimodal Foundation Models

We first evaluate the interpretative performance of our attribution method on multimodal foundation models, including CLIP [27], ImageBind [28], and LanguageBind [29]. We select 5,000 correctly predicted ImageNet images for each model for validation. Table 1 presents the faithfulness results across various attribution

methods, with our approach demonstrating strong attribution effectiveness. The attribution results on CLIP (ViT-L) show that, compared to the state-of-the-art Grad-ECLIP [20], which is based on gradient and internal attention activation, our method achieves a 32.6% improvement in Deletion AUC score, a 61.8% improvement in Insertion AUC score, and a 4.0% improvement in μ Fidelity when using SLICO as the sub-region division algorithm. Fig. 4 qualitatively shows the saliency maps generated by different attribution methods on the CLIP model, where our approach effectively reduces noise and eliminates redundant regions, resulting in more interpretable and clearer attribution maps. On the ImageBind model, the Integrated Gradients [17] method produces better attribution results. In comparison, our method improves the Deletion AUC score by 9.8%, the Insertion AUC score by 33.8%, and the μ Fidelity by 85.0% when using the SLICO sub-region division algorithm. For LanguageBind, our approach outperforms the perturbation-based HSIC-Attribution [9] method by 43.9% in the Deletion AUC score and 48.8% in the Insertion AUC score when using SLICO as the sub-region division algorithm. Although our method is slightly lower by 0.9% in the μ Fidelity metric, it still demonstrates strong attribution capability. Compared to the previous version, our method improves the Insertion AUC scores by 10.2%, 12.2%, and 19.2% and the Deletion AUC scores by 31.5%, 7.1%, and 27.5% across the three models, respectively, demonstrating that attribution results based on semantic division are more effective.

We also validated our attribution method on the CLIP model with ResNet-101 as the backbone, as shown in Table 2. Our approach outperforms the state-of-the-art perturbation-based HSIC-Attribution method by 31.9% in the Deletion AUC score and 51.8% in the Insertion AUC score when using SLICO as the sub-region division algorithm. Although it does not achieve the best results in the μ Fidelity metric, the performance on the first two metrics demonstrates that our method more effectively identifies the most critical combination of decision regions. Compared with the previous version of the method, the Insertion and Deletion AUC scores increased by 21.3% and 8.4%, respectively.

From Tables 1 and 2, we observe that comparable performance can be achieved when using SLICO as the division method. However, when using Segment Anything (SAM) for sub-region division, although it remains competitive compared to other attribution methods, there are noticeable performance differences relative to superpixel-based methods. This is mainly because SAM occasionally segments sub-regions that are too large, lacking fine-grained detail, and may include areas that negatively impact the results. Optimizing SAM for more fine-grained segmentation will be a focus of future work, which could lead to improved performance.

Fig. 5 shows the interpretation results for different multimodal foundation models on the ImageNet dataset. In the CLIP model attribution results, both Grad-ECLIP and our method accurately located the horse chestnut seed. However, Grad-ECLIP’s response jittered as key regions were revealed, while ours remained stable. Additionally, the region searched by our method achieved higher confidence, demonstrating its superiority. In the ImageBind model, the watermark affected the HSIC-Attribution method, causing it to misattribute the location and miss the chameleon, leading to poor faithfulness. In contrast, our method successfully identifies the area where ImageBind accurately recognizes the chameleon category. An interesting phenomenon occurs in LanguageBind: while the HSIC-Attribution method seems to more effectively locate the

TABLE 1
Deletion, Insertion AUC scores and μ Fidelity for multimodal ViT backbone foundation models on the ImageNet validation sets.

Methods	CLIP (ViT-L) [27]			ImageBind (Huge) [28]			LanguageBind (Large) [29]		
	Deletion (\downarrow)	Insertion (\uparrow)	μ Fidelity (\uparrow)	Deletion (\downarrow)	Insertion (\uparrow)	μ Fidelity (\uparrow)	Deletion (\downarrow)	Insertion (\uparrow)	μ Fidelity (\uparrow)
Saliency [37]	0.3040	0.1938	0.1010	0.3857	0.3473	0.1807	0.2237	0.2379	0.2395
Integrated Gradients [17]	0.1600	0.3560	0.0881	0.1405	0.5577	0.1919	0.0699	0.2733	0.1422
iGOS++ [19]	0.2934	0.4467	0.2313	0.2658	0.4417	0.2371	-	-	-
RISE [23]	0.1615	0.5345	0.3244	0.1528	0.4699	0.3459	0.1145	0.4750	0.2764
HSIC-Attribution [9]	0.1565	0.4397	0.3232	0.1875	0.4407	0.3413	0.1034	0.4070	0.4132
Kernel SHAP [21]	0.2808	0.3588	0.0699	0.3736	0.4714	0.0931	0.2104	0.3109	0.0998
ViT-CX [41]	0.1779	0.4413	0.2076	0.1987	0.4277	0.3377	0.1303	0.3486	0.1015
EAC [22] (w/ Segment Anything)	0.3792	0.4349	0.1566	0.3888	0.4564	0.2740	0.1563	0.4340	0.2848
Grad-ECLIP [20]	0.1374	0.4783	0.3205	-	-	-	-	-	-
Previous work [8]	0.1351	0.6752	-	0.1378	0.6652	-	0.0885	0.5082	-
LiMA (w/ Segment Anything)	0.1905	0.7151	0.2953	0.2210	0.7341	0.3492	0.2228	0.6690	0.3648
LiMA (w/ SLICO)	0.0926	0.7441	0.3334	0.1280	0.7463	0.3551	0.0642	0.6058	0.4096

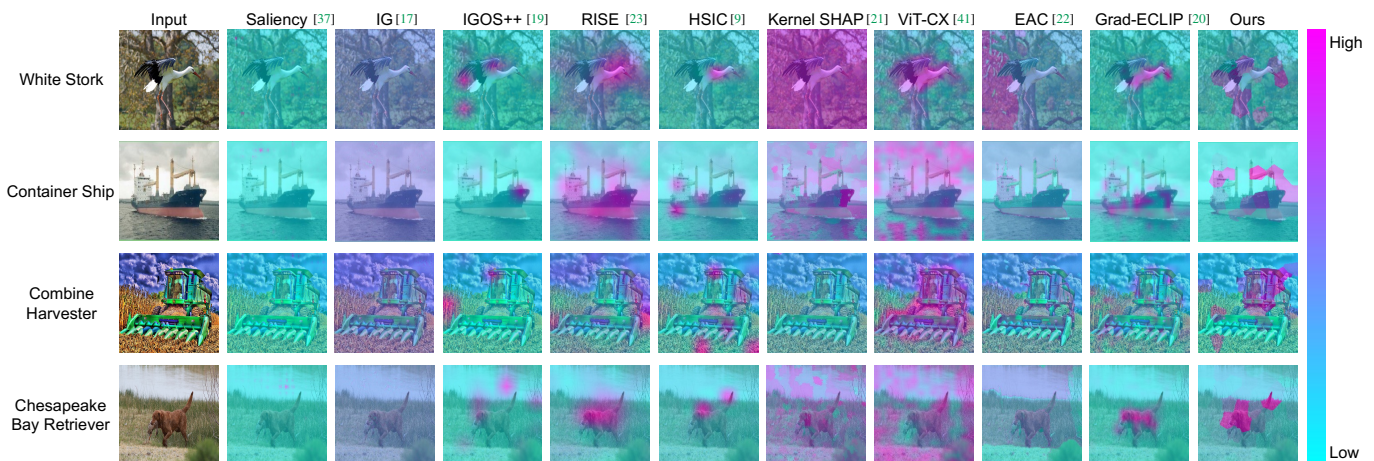


Fig. 4. Visual explanations of the CLIP model using various attribution mechanisms, with our approach effectively reducing noise and eliminating redundant regions, leading to more interpretable attribution results.

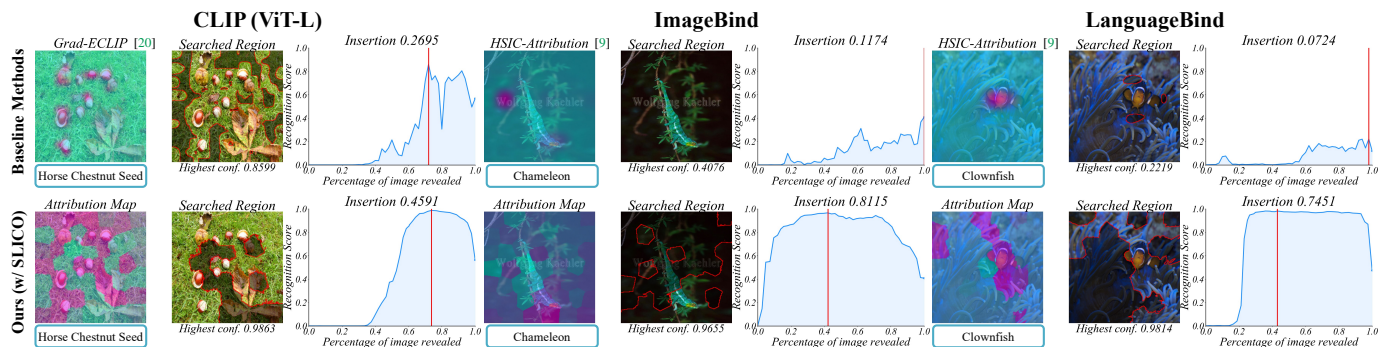


Fig. 5. Attribution visualizations of decision results for different multimodal foundation models on the ImageNet dataset. The first row shows the interpretation results from the state-of-the-art baseline attribution methods, while the second row displays the interpretation results from our method. Each interpretation result includes the saliency map, the highest confidence score, and its corresponding region, as well as the Insertion AUC curve. The red line in the curve represents the highest confidence of the model's response during the search.

clownfish, the model shows no positive response as key regions are revealed. Our method, however, identifies both the clownfish and surrounding background regions, enabling the model to recognize the category more effectively. This highlights the gap between human cognition and machine learning, illustrating why humans alone cannot evaluate attribution effectiveness. Please refer to the supplementary material B.2 for more visualization results.

By reformulating the image attribution problem as a subset selection problem, we effectively address the issue of insufficient granularity in the attribution region, making our approach better suited for explaining models with complex interactive responses. As a result, our method significantly improves faithfulness com-

pared to existing attribution algorithms.

6.3.2 Faithfulness on Single-Modal Models

We also validate the effectiveness of our explanation method on single-modal models, including CNN, Vision Transformer, and Vision Mamba architectures. For each model, we select 5,000 correctly predicted ImageNet images.

Faithfulness on CNN: We select the ResNet-101 [73] pre-trained on ImageNet to verify the effectiveness of our method. Table 3 presents the attribution performance of various methods, where our approach outperforms the state-of-the-art perturbation-based HSIC-Attribution method by 34.5% in the Deletion AUC

TABLE 2
Deletion, Insertion AUC scores and μ Fidelity for CLIP model with ResNet-101 backbone on the ImageNet validation sets.

Methods	CLIP (ResNet-101) [27]		
	Deletion (\downarrow)	Insertion (\uparrow)	μ Fidelity (\uparrow)
Saliency [37]	0.0801	0.1540	0.3648
Integrated Gradients [17]	0.0482	0.0804	0.1141
Kernel SHAP [21]	0.1198	0.1766	0.0923
RISE [23]	0.0719	0.4034	0.3355
HSIC-Attribution [9]	0.0659	0.3574	0.4373
EAC [22] (w/ Segment Anything)	0.2332	0.2756	0.2463
Previous work [8]	0.0490	0.4474	-
LiMA (w/ SLICO)	0.0449	0.5427	0.3827

score and 47.0% in the Insertion AUC score when using SLICO as the sub-region division algorithm. Compared with the previous version of the method, the Insertion and Deletion AUC scores increased by 29.1% and 11.8%, respectively. This demonstrates that our method is highly competitive on the CNN models. Please refer to the supplementary material B.2 for the visualization results.

TABLE 3
Deletion and Insertion AUC scores for single modal ResNet-101 backbone on the ImageNet validation sets.

Methods	ResNet-101 [73]		
	Deletion (\downarrow)	Insertion (\uparrow)	μ Fidelity (\uparrow)
Saliency [37]	0.1148	0.2613	0.4556
Integrated Gradients [17]	0.0521	0.1482	0.1822
iGOS++ [19]	0.1934	0.3779	0.3377
Kernel SHAP [21]	0.1944	0.2878	0.1399
RISE [23]	0.1101	0.4920	0.3827
HSIC-Attribution [9]	0.0866	0.4448	0.5805
Previous work [8]	0.0643	0.5063	-
LiMA (w/ SLICO)	0.0567	0.6538	0.4203

Faithfulness on Vision Transformer: To validate the effectiveness of our method on transformer backbones, we employed the Vision Transformer-Large (ViT-L) [74] and Swin Transformer-Large (Swin-L) [75], both pre-trained on ImageNet. Table 4 presents the attribution performance, where RISE [23] proves to be a strong baseline method for ViT backbones. Compared to RISE, our method outperforms both the ViT-L and Swin-L models, achieving a 48.9% and 56.4% improvement in the Deletion AUC score and a 19.9% and 34.9% improvement in the Insertion AUC score, respectively. Compared with the previous version of the method, the Insertion and Deletion AUC scores increased by 11.1% and 33.2% on average, respectively. Please refer to the supplementary material B.3 for the visualization results.

TABLE 4
Deletion and Insertion AUC scores for single modal vision transformer backbones on the ImageNet validation sets.

Methods	ViT-L [74]		Swin-L [75]	
	Deletion (\downarrow)	Insertion (\uparrow)	Deletion (\downarrow)	Insertion (\uparrow)
Saliency [37]	0.3499	0.3544	0.2888	0.4178
Integrated Gradients [17]	0.1530	0.2402	0.3074	0.4198
Kernel SHAP [21]	0.4155	0.4942	0.4300	0.4794
RISE [23]	0.1947	0.6177	0.3338	0.5655
HSIC-Attribution [9]	0.1898	0.5253	0.3589	0.5531
Previous work [8]	0.1268	0.6715	0.2490	0.6811
LiMA (w/ SLICO)	0.0994	0.7405	0.1371	0.7627

Faithfulness on Vision Mamba: To evaluate the effectiveness of our attribution method on the latest Mamba architecture, we tested it on Vision Mamba (base) [76] and MambaVision (L2) [77], both pre-trained on ImageNet. As shown in Table 5, RISE remains a robust baseline method among the comparisons.

However, our method demonstrated superior performance, surpassing RISE on both the Vision Mamba (base) and MambaVision (L2) models with a 58.9% and 59.8% increase in Deletion AUC score, and a 30.0% and 25.3% improvement in Insertion AUC score, respectively. Compared with the previous version of the method, the Insertion and Deletion AUC scores increased by 14.3% and 37.6%, respectively. Please see the supplementary material B.4 for the visualization results.

TABLE 5
Deletion and Insertion AUC scores for single modal mamba backbones on the ImageNet validation sets.

Methods	Vision Mamba (base) [76]		MambaVision (L2) [77]	
	Deletion (\downarrow)	Insertion (\uparrow)	Deletion (\downarrow)	Insertion (\uparrow)
Saliency [37]	0.2793	0.1938	0.1681	0.1494
Integrated Gradients [17]	0.0914	0.2323	0.1067	0.2202
Kernel SHAP [21]	0.2947	0.3603	0.2030	0.2345
RISE [23]	0.2008	0.5352	0.1419	0.2937
HSIC-Attribution [9]	0.2067	0.4872	0.1541	0.2753
Previous work [8]	0.1387	0.6281	0.0872	0.3121
LiMA (w/ SLICO)	0.0825	0.6957	0.0570	0.3680

In summary, our interpretable approach demonstrates strong attribution performance and generalizes well across models with different architectures.

6.3.3 Faithfulness on Face Recognition Models

Table 6 shows the results on the Celeb-A and VGG-Face2 validation sets. On the Celeb-A dataset, our method surpasses the state-of-the-art HSIC-Attribution [9] approach, achieving a 42.0% improvement in Deletion AUC, a 5.9% increase in Insertion AUC, and a 9.0% enhancement in μ Fidelity. Similarly, on the VGG-Face2 dataset, our method outperforms HSIC-Attribution with gains of 46.3% in Deletion AUC, 2.2% in Insertion AUC, and 1.2% in μ Fidelity. In addition, compared to the previous version [8], our method improves the Deletion AUC score by 36.4% and the Insertion AUC score by 4.8% on the Celeb-A dataset. On the VGG-Face2 dataset, it achieves improvements of 45.8% in the Deletion AUC score and 2.0% in the Insertion AUC score. Compared to the previous large-scale pre-trained models validated on the ImageNet dataset, the improvement is less pronounced. This is primarily due to the fact that face recognition images are aligned, resulting in fewer complex interaction effects than those encountered in large-scale pre-trained models. Nevertheless, our method shows consistent improvement over the baseline and achieves state-of-the-art performance.

TABLE 6
Deletion, Insertion AUC scores, and μ Fidelity on the Celeb-A and VGG-Face2 validation sets.

Methods	Celeb-A (ArcFace ResNet-101)			VGGFace2 (ArcFace ResNet-101)		
	Deletion (\downarrow)	Insertion (\uparrow)	μ Fidelity (\uparrow)	Deletion (\downarrow)	Insertion (\uparrow)	μ Fidelity (\uparrow)
Saliency [37]	0.1453	0.4632	0.3258	0.1907	0.5612	0.5034
Grad-CAM [18]	0.2865	0.3721	0.0672	0.3103	0.4733	0.2773
Integrated Gradients [17]	0.0680	0.3578	0.3352	0.0749	0.5399	0.3853
LIME [45]	0.1484	0.5246	0.1985	0.2034	0.6185	0.4856
Kernel SHAP [21]	0.1409	0.5246	0.2722	0.2119	0.6132	0.4905
RISE [23]	0.1444	0.5703	0.4147	0.1375	0.6530	0.3822
HSIC-Attribution [9]	0.1151	0.5692	0.5530	0.1317	0.6694	0.5295
Previous work [8]	0.1054	0.5752	-	0.1304	0.6705	-
LiMA (w/ SLICO)	0.0668	0.5849	0.5743	0.0707	0.6841	0.5361

6.3.4 Faithfulness on A Fine-grained Model

Table 7 shows the results on the CUB-200-2011 validation sets. Compared to the state-of-the-art HSIC-Attribution [9] method, our approach surpasses it by 13.44% in Deletion AUC score, 13.22% in Insertion AUC score, and achieves a 3.3% improvement in μ Fidelity. Additionally, compared to the previous version [8], our method improves the Deletion AUC score by 8.6% and the

TABLE 7
Deletion, Insertion AUC scores, and μ Fidelity on the CUB-200-2011 validation set.

Methods	CUB-200-2011		
	Deletion (\downarrow)	Insertion (\uparrow)	μ Fidelity (\uparrow)
Saliency [37]	0.0682	0.6585	0.1409
Grad-CAM [18]	0.0810	0.7224	0.1486
Integrated Gradients [17]	0.1693	0.5263	0.2832
LIME [45]	0.1070	0.6812	0.0948
Kernel SHAP [21]	0.1016	0.6763	0.1452
RISE [23]	0.0665	0.7193	0.2370
HSIC-Attribution [9]	0.0647	0.6843	0.3435
Previous work [8]	0.0613	0.7262	-
LIMA (w/ Segment Anything)	0.0829	0.7106	0.3420
LIMA (w/ SLICO)	0.0560	0.7748	0.3547

Insertion AUC score by 6.7%. The CUB-200-2011 dataset is a single-object dataset, meaning the model correctly predicts with fewer sub-region complex interaction effects, but our method still delivers highly competitive results.

6.3.5 Faithfulness on Audio Recognition Model

Explanation and transparency are important issues to ethical AI for music and audio [82], yet there is limited existing research on explaining audio classification. In this section, we analyze audio classification explanations from the perspective of spectrograms, utilizing two multi-modal foundation models. For sub-region division, we adopt a patch-based approach. Table 8 presents the attribution results of our method compared to the baseline on the VGG-Sound [32] dataset. On ImageBind, the Square-Grad [83] method is notably competitive, but our approach surpasses it by 56.0% in Deletion AUC and 83.9% in Insertion AUC when using a 10×10 patch sub-region division. On LanguageBind, the RISE [23] method performs well, yet our method exceeds it by 42.8% in Deletion AUC and 79.6% in Insertion AUC. Although Integrated Gradients [17] achieves the best Deletion AUC score, our method delivers strong performance overall, with Integrated Gradients performing poorly on the Insertion AUC. We demonstrate the robust attribution capability of our method on the Audio modality, highlighting its adaptability across different modalities. Fig. 6 presents the attribution visualization results on the spectrogram, highlighting the regions the model focuses on for classification. Future work will explore ways to enhance human understanding of these interpretation results.

TABLE 8
Deletion and Insertion AUC scores for multimodal ViT backbones on the VGG-Sound validation sets.

Methods	ImageBind [28]		LanguageBind [29]	
	Deletion (\downarrow)	Insertion (\uparrow)	Deletion (\downarrow)	Insertion (\uparrow)
Saliency [37]	0.0999	0.1823	0.1024	0.2184
Gradient-Input [84]	0.0326	0.1257	0.0243	0.1388
SmoothGrad [85]	0.0734	0.0955	0.0535	0.1664
Integrated Gradients [17]	0.0313	0.1292	0.0165	0.2153
VarGrad [86]	0.0755	0.2121	0.0955	0.2643
Square-Grad [83]	0.0748	0.2120	0.0888	0.2697
LIME [45]	0.1375	0.1422	0.1092	0.2164
Kernel SHAP [21]	0.1316	0.1436	0.1456	0.1785
Occlusion [87]	0.0707	0.1650	0.0911	0.2052
RISE [23]	0.0782	0.1952	0.0800	0.2879
Sobol-Attribution [88]	0.0881	0.1429	0.0956	0.2235
HSIC-Attribution [9]	0.0891	0.1418	0.0904	0.2270
LIMA (8×8)	0.0425	0.4164	0.0806	0.5362
LIMA (10×10)	0.0329	0.3899	0.0458	0.5172

6.4 Discover the Causes of Incorrect Predictions

In this section, we aim to analyze the misclassified images and assess whether the attribution algorithm can accurately identify the causes of the model’s prediction errors. We use the Average Highest Confidence within a limited search region (*e.g.*, reveal up to 25% of the image region) and the Insertion AUC score as our

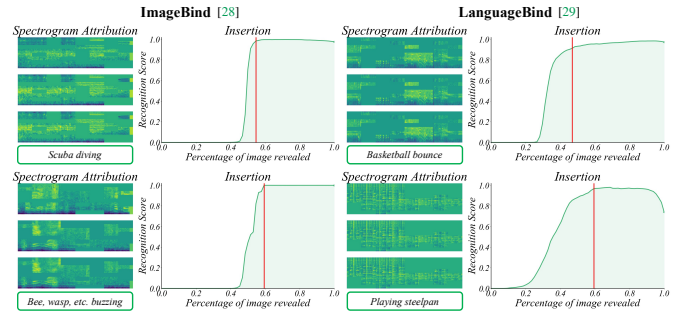


Fig. 6. Attribution visualizations for audio classification on ImageBind and LanguageBind, highlighting the most critical spectrogram regions attributed to the model. Additionally, we provide the corresponding Insertion AUC curve.

evaluation metrics. The Deletion AUC score is not considered, as the initial prediction scores for the misclassified samples are already very low. We validate our method on the ImageNet [31], CUB-200-2011 [33], VGG-Sound [32], and LC25000 (Lung) [36] datasets. The ground truth labels are given.

6.4.1 Attributing Multimodal Foundation Model Errors

We first analyzed the samples misclassified by the multimodal foundation models. Table 9 presents the attribution results for these misclassified samples, using the ground truth labels for interpretation. Our approach achieved stunning results. When utilizing Segment Anything (SAM) [65] as the sub-region division algorithm, our method outperforms RISE [23] by 61.5% on the CLIP (ViT-L) model and 52.4% on ImageBind, while surpassing EAC [22] by 63.8% on LanguageBind in terms of the average highest confidence during the global search. For Insertion metrics, our method exceeds RISE [23] by 127.2% on CLIP (ViT-L) and 89.4% on ImageBind, and outperforms EAC [22] by 101.9% on LanguageBind.

TABLE 9
Evaluation on discovering the cause of incorrect predictions for different multimodal models on ImageNet dataset.

Backbones	Methods	Average highest confidence (\uparrow)				Insertion (\uparrow)
		(0-25%)	(0-50%)	(0-75%)	(0-100%)	
CLIP (ViT-L) [27]	RISE [23]	0.2710	0.3985	0.4558	0.4879	0.1827
	HSIC-Attribution [9]	0.2148	0.2723	0.3051	0.3462	0.1062
	ViT-CX [41]	0.1268	0.2367	0.3137	0.3902	0.1236
	EAC [22] (w/ Segment Anything)	0.1004	0.1861	0.2561	0.3397	0.1086
	Grad-ECLIP [20]	0.2202	0.3404	0.3767	0.4123	0.1397
	Previous work [8]	0.2012	0.3073	0.3582	0.3989	0.2017
	LIMA (w/ SLICO)	0.5677	0.7030	0.7479	0.7583	0.4789
	LIMA (w/ Segment Anything)	0.6640	0.7307	0.7676	0.7878	0.4151
ImageBind [28]	RISE [23]	0.2427	0.4045	0.4757	0.5164	0.2237
	HSIC-Attribution [9]	0.1711	0.2726	0.3260	0.3636	0.2180
	ViT-CX [41]	0.1299	0.2593	0.3532	0.4261	0.1129
	EAC [22] (w/ Segment Anything)	0.1064	0.1901	0.2658	0.3463	0.1124
	Previous work [8]	0.4436	0.5865	0.6157	0.6348	0.3929
	LIMA (w/ SLICO)	0.5351	0.6816	0.7445	0.7557	0.4681
	LIMA (w/ Segment Anything)	0.6639	0.7487	0.7736	0.7872	0.4237
	LanguageBind [29]	RISE [23]	0.0967	0.1902	0.2530	0.2920
HSIC-Attribution [9]		0.0787	0.1380	0.1779	0.2112	0.0861
ViT-CX [41]		0.0414	0.1123	0.1628	0.2348	0.0816
EAC [22] (w/ Segment Anything)		0.1404	0.2802	0.3755	0.4245	0.1721
Previous work [8]		0.2050	0.2933	0.3360	0.3506	0.1812
LIMA (w/ SLICO)		0.3843	0.5311	0.5824	0.5978	0.3483
LIMA (w/ Segment Anything)		0.5401	0.6399	0.6753	0.6955	0.3475

This is primarily due to the presence of potential regions in the samples where the model predicts incorrectly, which exerts a strong influence on the model’s decision, leading to complex interactions between features. Traditional attribution algorithms struggle to effectively identify these regions. In contrast, our method leverages marginal contribution scores, enabling it to attribute regions that are more relevant to the target class and pinpoint the causes of the model’s incorrect predictions. Therefore, our method achieves more competitive results than the baseline method on such samples.

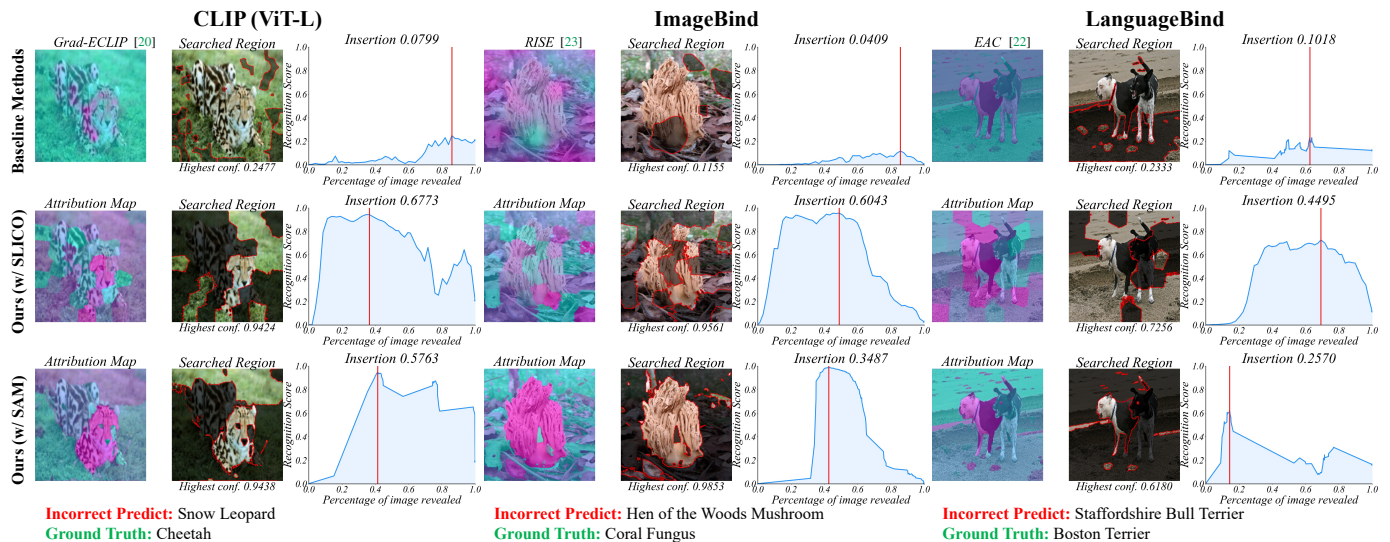


Fig. 7. Visualization of the method for discovering what causes foundation model prediction errors. The Insertion curve shows the correlation between the searched region and ground truth class prediction confidence. The highlighted region matches the searched region indicated by the red line in the curve, and the dark region is the error cause identified by the method.

TABLE 10

Evaluation on discovering the cause of incorrect predictions for different multimodal models on the VGG-Sound dataset.

Backbones	Methods	Average highest confidence (\uparrow)				Insertion (\uparrow)
		(0-25%)	(0-50%)	(0-75%)	(0-100%)	
ImageBind [28]	Integrated Gradients [17]	0.0081	0.0318	0.0776	0.3904	0.0460
	RISE [23]	0.0064	0.0533	0.1547	0.2546	0.0385
	HSIC-Attribution [9]	0.0107	0.0441	0.0609	0.1657	0.0201
	LiMA (10 \times 10)	0.0955	0.1978	0.3992	0.5028	0.1813
LanguageBind [29]	Integrated Gradients [17]	0.0574	0.1092	0.1747	0.4254	0.1153
	RISE [23]	0.0478	0.1415	0.2283	0.2799	0.1001
	HSIC-Attribution [9]	0.0365	0.0711	0.1213	0.1821	0.0532
	LiMA (10 \times 10)	0.2656	0.4195	0.5543	0.5767	0.3022

TABLE 11

Evaluation on discovering the cause of incorrect predictions for medical multimodal model QuiltNet on LC25000 (Lung) dataset.

Backbone	Methods	Average highest confidence (\uparrow)				Insertion (\uparrow)
		(0-25%)	(0-50%)	(0-75%)	(0-100%)	
QuiltNet (ViT/B-32) [30]	Integrated Gradients [17]	0.2989	0.2989	0.2989	0.3012	0.1344
	Kernel SHAP [21]	0.1957	0.1962	0.1965	0.2024	0.1359
	RISE [23]	0.4986	0.5109	0.5163	0.5171	0.1470
	HSIC-Attribution [9]	0.4858	0.4927	0.5005	0.5013	0.1468
	ViT-CX [41]	0.3497	0.3595	0.3637	0.3658	0.1419
	LiMA (w/ SLICO)	0.6215	0.6764	0.6901	0.6915	0.3401

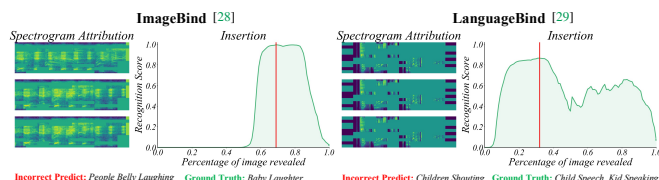


Fig. 8. Visualization of the method for discovering what causes audio recognition model prediction errors.

Fig. 7 shows some visualization results, we compare our method with strong baseline methods on different foundation models. The Insertion curve represents the relationship between the region searched by the methods and the ground truth class prediction confidence. We find that our method can search for regions with higher confidence scores predicted by the model than the SOTA methods with a small percentage of the searched image region. The highlighted region shown in the figure can be considered as the cause of the correct prediction of the model, while the dark region is the cause of the incorrect prediction of the model. This also demonstrates that our method can achieve higher interpretability with fewer fine-grained regions.

Additionally, we observed that for the average highest confidence metric, using SAM as the sub-region division algorithm yields better results, while the superpixel-based division method performs better for the Insertion metric. This is mainly because the sub-regions generated by SAM have stronger semantic coherence, giving it an advantage when identifying regions of high model interest. However, SAM sometimes produces sub-regions that are too large and uncontrollable, leading to mixed positive and negative regions in one sub-region. As a result, it performs slightly worse than the superpixel-based method for the Insertion metric.

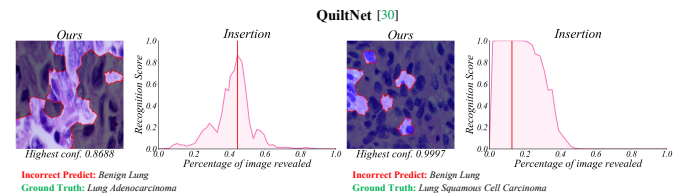


Fig. 9. Visualization of the method for discovering what causes medical foundation model prediction errors.

6.4.2 Attributing Audio Foundation Model Errors

Next, we validate our approach on the audio modality by attributing misclassified audio samples and analyzing the spectrogram regions responsible for prediction errors. Table 10 presents the attribution results on ImageBind [28] and LanguageBind [29]. Our method outperforms RISE by 28.8% and 35.6% in average highest confidence on the ImageBind and LanguageBind models, respectively. For the Insertion AUC score, it surpasses RISE by 294.1% on ImageBind and 162.1% on LanguageBind, demonstrating the strong generalizability of our method across different modalities. Fig. 8 illustrates the attribution results of our method on misclassified audio samples. By correctly searching the relevant spectral region, our method enables the model to make accurate predictions and reveals the spectrogram region responsible for the corrected prediction.

6.4.3 Attributing Medical Foundation Model Errors

We also evaluated our method's ability to attribute errors on the medical multimodal foundation model, QuiltNet [30]. Table 11 presents the attribution results. Compared to the HSIC-Attribution method, our approach improves the average highest confidence by 39.2% and the Insertion AUC score by 137.5%, demonstrating

strong attribution capabilities in the medical imaging domain. Fig. 9 shows images misclassified as Benign Lung by QuiltNet. Our method identifies key regions that trigger a strong response from the model for the correct category, thus interpreting the sources of the prediction errors.

6.4.4 Attributing Fine-graininess Recognition Model Errors

Finally, we evaluated our method’s ability to detect errors on fine-grained datasets across three CNN models. Table 12 presents the results for misclassified samples from the CUB-200-2011 [33] validation set, where our method demonstrates significant improvements. Compared to the state-of-the-art HSIC-Attribution method, in the global search interval (0-100%), the average highest confidence identified by our method increased by 217.5% on ResNet-101, 152.2% on MobileNetV2, and 123.9% on EfficientNetV2-M, when using SAM as the sub-region division method. Similarly, the Insertion AUC score saw substantial improvements, increasing by 178.7% on ResNet-101, 101.7% on MobileNetV2, and 139.4% on EfficientNetV2-M. In addition, compared to the previous version of our method, we achieved improvements of 75.4%, 36.9%, and 81.5% in the average highest confidence on the three CNN models, and 127.4%, 71.5%, and 120.7% in the Insertion AUC score, respectively. See the supplementary material C for the visualization results.

TABLE 12

Evaluation on discovering the cause of incorrect predictions for different convolutional neural network backbones on CUB-200-2011 dataset.

Backbones	Methods	Average highest confidence (%)				
		(0-25%)	(0-50%)	(0-75%)	(0-100%)	Insertion (†)
ResNet-101 [73]	Grad-CAM++ [39]	0.1988	0.2447	0.2544	0.2647	0.1094
	Score-CAM [40]	0.1896	0.2323	0.2449	0.2510	0.1073
	Kernel SHAP [21]	0.0983	0.0247	0.0574	0.2642	0.1098
	RISE [23]	0.2406	0.3092	0.3316	0.3807	0.2238
	HSIC-Attribution [9]	0.1709	0.2091	0.2250	0.2493	0.1446
	Previous work [8]	0.2430	0.3519	0.3984	0.4513	0.1772
	LiMA (w/ SLICO)	0.3683	0.5016	0.5501	0.6003	0.3694
LiMA (w/ Segment Anything)	0.3874	0.4957	0.5975	0.7916	0.4030	
MobileNetV2 [78]	Grad-CAM++ [39]	0.1584	0.2820	0.3223	0.3462	0.1284
	Score-CAM [40]	0.1574	0.2456	0.2948	0.3141	0.1195
	Kernel SHAP [21]	0.0525	0.1367	0.2321	0.4142	0.2511
	RISE [23]	0.2340	0.3101	0.3355	0.4280	0.2573
	HSIC-Attribution [9]	0.1648	0.2190	0.2415	0.2914	0.1635
	Previous work [8]	0.2460	0.4142	0.4913	0.5367	0.1922
	LiMA (w/ SLICO)	0.3466	0.4686	0.5462	0.6278	0.3448
LiMA (w/ Segment Anything)	0.5339	0.6098	0.6611	0.7349	0.3297	
EfficientNetV2-M [79]	Grad-CAM++ [39]	0.2338	0.2549	0.2598	0.2659	0.1605
	Score-CAM [40]	0.2126	0.2327	0.2375	0.2403	0.1572
	Kernel SHAP [21]	0.0123	0.0670	0.1489	0.3357	0.0787
	RISE [23]	0.2958	0.3339	0.3473	0.3697	0.2274
	HSIC-Attribution [9]	0.2418	0.2561	0.2615	0.2679	0.1611
	Previous work [8]	0.2616	0.3117	0.3235	0.3306	0.1748
	LiMA (w/ SLICO)	0.3670	0.4575	0.4799	0.4859	0.3518
LiMA (w/ Segment Anything)	0.4138	0.5035	0.5543	0.5999	0.3857	

We found that our method’s ability to attribute misclassified samples on the CUB-200-2011 dataset is significantly higher than its performance on correctly classified samples. This is primarily because correctly predicted samples in this dataset typically lack complex interaction effects, whereas misclassified samples often involve potential causal confusion and exhibit more intricate feature interactions. As our method is well-suited to handling complex feature interactions, it shows a distinct advantage in attributing misclassified samples compared to the baseline method.

6.5 Ablation Study

In this section, we provide a comprehensive ablation study of the various components of our approach, conducted on the ImageBind model and the ImageNet dataset, and the sub-region division algorithm is SLICO.

6.5.1 Ablation of the Bidirectional Greedy Search Algorithm

In Section 4.3, we analyzed the optimal bounds and inference number optimization of the proposed bidirectional greedy search algorithm from a theoretical perspective. We conduct a series of

ablation studies, as shown in Table 13. Although the naive greedy algorithm delivers the best performance, it still requires a considerable amount of time to run. By implementing the bidirectional greedy search strategy, we significantly reduce the number of model inferences, leading to a substantial decrease in attribution time. The time complexity of this approach is influenced by the hyperparameter n_p . While a larger n_p increases the search duration, it also enhances attribution performance, highlighting a trade-off between speed and accuracy. Our experiments indicate that setting n_p to 8 strikes an effective balance, providing strong attribution performance while reducing the runtime to 62.5% of the original.

TABLE 13

Ablation study on the bidirectional greedy search algorithm for ImageBind on the ImageNet dataset.

Bi-directional subset	Num. of neg. samples n_p	Faithfulness metrics			Exec. time (s)
		Deletion (↓)	Insertion (↑)	μ Fidelity (†)	
✗	0	0.1260	0.8099	0.3669	32
✓	1	0.2048	0.6445	0.3344	16
✓	4	0.1309	0.7303	0.3508	18
✓	8	0.1280	0.7463	0.3526	20
✓	12	0.1271	0.7517	0.3551	22
✓	16	0.1269	0.7542	0.3471	25

6.5.2 Ablation of the Submodular Function

We analyzed the impact of various submodular function-based score functions. We conducted ablation studies on both correctly predicted and incorrectly predicted samples.

Impact on correctly predicting samples: As shown in Table 14, using a single score function within the submodular framework limits the faithfulness of attribution. However, combining score functions in pairs leads to improved faithfulness. Our results show that removing any of the four score functions results in degraded Deletion and Insertion scores, confirming the importance of each function. Notably, the consistency and collaboration scores have a greater impact on attribution, while the confidence and effectiveness scores serve a more constraining role. This is reflected in why larger weights are assigned to the first two functions during hyperparameter tuning.

TABLE 14

Ablation study on components of different score functions of submodular function for ImageBind on the ImageNet dataset.

Submodular Function				Deletion (↓)	Insertion (†)
Cons. Score (Equation 3)	Colla. Score (Equation 4)	Conf. Score (Equation 5)	Eff. Score (Equation 7)		
✓	✗	✗	✗	0.2567	0.6324
✗	✓	✗	✗	0.1031	0.5598
✗	✗	✓	✗	0.3416	0.3609
✗	✗	✗	✓	0.3267	0.3909
✓	✓	✗	✗	0.1290	0.7403
✗	✓	✓	✗	0.1022	0.5520
✗	✗	✓	✓	0.2861	0.4465
✗	✓	✓	✓	0.1115	0.5595
✓	✗	✓	✓	0.2570	0.6432
✓	✓	✗	✓	0.1293	0.7436
✓	✓	✓	✗	0.1333	0.7442
✓	✓	✓	✓	0.1280	0.7463

Impact on incorrectly predicting samples: We primarily focus on the impact of the consistency score and collaboration score on the attribution of misclassified samples. As shown in Table 15, removing any score function leads to a decrease in both the average highest confidence and the Insertion AUC score. This indicates that even for attribution on misclassified samples, both the consistency and collaboration scores are essential. Maximum performance is only achieved when both scores are used together.

TABLE 15
Ablation study on submodular function score components for incorrectly predicted samples for ImageBind on the ImageNet dataset.

Cons. Score (Equation 3)	Colla. Score (Equation 4)	Average highest confidence (\uparrow)				Insertion (\uparrow)
		(0-25%)	(0-50%)	(0-75%)	(0-100%)	
\times	\checkmark	0.0821	0.3075	0.5869	0.6113	0.2691
\checkmark	\times	0.5033	0.6087	0.6183	0.6392	0.2949
\checkmark	\checkmark	0.5351	0.6816	0.7445	0.7557	0.4681

6.5.3 Ablation on Importance Assessment

In this section, we perform an ablation study on the importance assessment method. The baseline for comparison assumes that the importance difference between adjacent sequence elements in the subset is consistent and equal to 1. We use μ Fidelity as the evaluation metric to assess the rationality of the importance score assignment. As shown in Table 16, we found that when evaluating the importance of each element in the subset, the μ Fidelity score improves relative to the baseline. This improvement demonstrates, to some extent, the validity of the importance scores assigned by this assessment strategy. Fig. 16A shows an attribution result, highlighting the search region at the inflection point of the Insertion curve, considered the most important. Fig. 16B and 16C illustrate different importance assessment strategies, showing that the proposed method helps users intuitively identify key regions.

TABLE 16
Ablation study on submodular function score components for incorrectly predicted samples for ImageBind on the ImageNet dataset.

Strategies	μ Fidelity (\uparrow)		
	CLIP (ViT-L)	ImageBind (Huge)	LanguageBind (Large)
Consistent subset difference	0.3208	0.3378	0.3889
Importance Assessment	0.3334	0.3551	0.4096

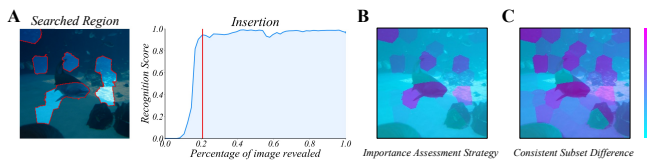


Fig. 10. An example of attribution results. **A.** Search region at the Insertion curve inflection point. **B.** Visualization using our strategy. **C.** Visualization using the baseline.

6.5.4 Ablation on Division Sub-region Number

The sub-region division algorithm plays a key role in determining the quality of the search space elements. In addition to the choice of algorithm, the number of sub-regions, denoted as $|V|$, is also an important factor. A higher number of sub-regions results in a more fine-grained division, but it also increases the attribution time. Therefore, this section examines the impact of the number of sub-regions on both performance and computation time. Similarly, we separately analyze the samples correctly and incorrectly predicted by the model.

Impact on correctly predicting samples: For samples correctly predicted by the model, the relationship between attribution performance and the number of sub-region divisions $|V|$ is shown in Table 17. We observed that as $|V|$ increases, attribution performance improves progressively, but the computation time rises significantly. Our method outperforms others when the number of sub-regions is set to 49. Future work should focus on improving the efficiency and accuracy of attribution when dealing with larger numbers of sub-regions.

Impact on incorrectly predicting samples: Next, for the samples the model predicted incorrectly, as shown in Table 18,

TABLE 17
Ablation study on the effect of sub-region division number $|V|$ for ImageBind on the ImageNet dataset.

Sub-region Number $ V $	Deletion (\downarrow)	Insertion (\uparrow)	μ Fidelity	Execution time (s)
49	0.1280	0.7463	0.3551	20
64	0.1230	0.7506	0.3473	39
77	0.1216	0.7532	0.3407	59
100	0.1199	0.7492	0.3291	158

our results indicate that dividing the image into more fine-grained sub-regions leads to higher average confidence scores (0-100%) and Insertion AUC scores. This further demonstrates that finer granularity in sub-region division results in better attribution performance.

TABLE 18
Ablation study on the effect of sub-region division number $|V|$ in incorrect sample attribution for ImageBind on the ImageNet dataset.

Sub-region Number $ V $	Average highest confidence (\uparrow)				Insertion (\uparrow)
	(0-25%)	(0-50%)	(0-75%)	(0-100%)	
49	0.5351	0.6816	0.7445	0.7557	0.4681
64	0.5579	0.7100	0.7689	0.7803	0.4934
77	0.5731	0.7194	0.7765	0.7884	0.5004
100	0.5987	0.7418	0.7958	0.8100	0.5144
121	0.6167	0.7599	0.8094	0.8247	0.5285

7 CONCLUSION

In this paper, we introduce LIMA, a novel and efficient black-box attribution method designed to tackle key challenges in understanding the behavior of AI systems. By identifying a diminishing marginal effect between inputs and outputs, we reformulate attribution as an optimization problem using submodular subset selection. This approach enables more faithful and interpretable attribution results with fewer input regions. Our proposed bidirectional greedy search algorithm significantly enhances attribution efficiency, allowing for the optimal identification of important regions while minimizing errors. Additionally, we observe that input interactions become increasingly complex as model pre-training scales grow, with higher parameter counts, more complex datasets, or in the presence of prediction errors. Our method is particularly well-suited to handle these challenging scenarios. We validate the effectiveness of LIMA across multiple datasets and multimodal models, achieving state-of-the-art performance. Notably, our method not only provides faithful explanations for correctly predicted samples but also delivers clear insights into the causes of the model’s incorrect predictions.

REFERENCES

- [1] A. Troncoso-García, M. Martínez-Ballesteros, F. Martínez-Álvarez, and A. Troncoso, “A new metric based on association rules to assess feature-attribution explainability techniques for time series forecasting,” *IEEE Transactions on Pattern Analysis and Machine Intelligence*, 2025. 1
- [2] Y. Rong, T. Leemann, T.-T. Nguyen, L. Fiedler, P. Qian, V. Unhelkar, T. Seidel, G. Kasneci, and E. Kasneci, “Towards human-centered explainable ai: A survey of user studies for model explanations,” *IEEE Transactions on Pattern Analysis and Machine Intelligence*, vol. 46, no. 4, pp. 2104–2122, 2024. 1
- [3] C. Patrício, J. C. Neves, and L. F. Teixeira, “Explainable deep learning methods in medical image classification: A survey,” *ACM Computing Surveys*, vol. 56, no. 4, pp. 1–41, 2023. 1
- [4] A. B. Arrieta, N. Díaz-Rodríguez, J. Del Ser, A. Bennetot, S. Tabik, A. Barbado, S. García, S. Gil-López, D. Molina, R. Benjamins *et al.*, “Explainable Artificial Intelligence (XAI): Concepts, taxonomies, opportunities and challenges toward responsible ai,” *Information fusion*, vol. 58, pp. 82–115, 2020. 1

- [5] R. Chen, J. Li, H. Zhang, C. Sheng, L. Liu, and X. Cao, "Sim2Word: Explaining similarity with representative attribute words via counterfactual explanations," *ACM Transactions on Multimedia Computing, Communications and Applications*, vol. 19, no. 6, pp. 1–22, 2023. **1**
- [6] Y. Gao, S. Gu, J. Jiang, S. R. Hong, D. Yu, and L. Zhao, "Going beyond XAI: A systematic survey for explanation-guided learning," *ACM Computing Surveys*, vol. 56, no. 7, pp. 1–39, 2024. **1**
- [7] L. Chen, P. Wu, K. Chitta, B. Jaeger, A. Geiger, and H. Li, "End-to-end autonomous driving: Challenges and frontiers," *IEEE Transactions on Pattern Analysis and Machine Intelligence*, vol. 46, no. 12, pp. 10 164–10 183, 2024. **1**
- [8] R. Chen, H. Zhang, S. Liang, J. Li, and X. Cao, "Less is more: Fewer interpretable region via submodular subset selection," in *ICLR*, 2024. **1, 2, 3, 4, 5, 9, 10, 11, 12, 14, 19, 22**
- [9] P. Novello, T. Fel, and D. Vigouroux, "Making sense of dependence: Efficient black-box explanations using dependence measure," in *NeurIPS*, 2022, pp. 4344–4357. **1, 3, 9, 10, 11, 12, 13, 14, 19, 21, 22, 23**
- [10] H. Deng, N. Zou, M. Du, W. Chen, G. Feng, Z. Yang, Z. Li, and Q. Zhang, "Unifying fourteen post-hoc attribution methods with Taylor interactions," *IEEE Transactions on Pattern Analysis and Machine Intelligence*, 2024. **1, 7**
- [11] R. Chen, S. Liang, J. Li, S. Liu, M. Li, Z. Huang, H. Zhang, and X. Cao, "Interpreting object-level foundation models via visual precision search," *arXiv preprint arXiv:2411.16198*, 2024. **1**
- [12] W.-J. Nam and S.-W. Lee, "Illuminating salient contributions in neuron activation with attribution equilibrium," *IEEE Transactions on Pattern Analysis and Machine Intelligence*, vol. 47, no. 2, pp. 1120–1131, 2025. **1**
- [13] S. Luo, H. Ivison, S. C. Han, and J. Poon, "Local interpretations for explainable natural language processing: A survey," *ACM Computing Surveys*, vol. 56, no. 9, pp. 1–36, 2024. **1**
- [14] H. Mandler and B. Weigand, "A review and benchmark of feature importance methods for neural networks," *ACM Computing Surveys*, vol. 56, no. 12, pp. 1–30, 2024. **1**
- [15] R. Dwivedi, D. Dave, H. Naik, S. Singhal, R. Omer, P. Patel, B. Qian, Z. Wen, T. Shah, G. Morgan *et al.*, "Explainable ai (xai): Core ideas, techniques, and solutions," *ACM Computing Surveys*, vol. 55, no. 9, pp. 1–33, 2023. **1**
- [16] S. Bach, A. Binder, G. Montavon, F. Klauschen, K.-R. Müller, and W. Samek, "On pixel-wise explanations for non-linear classifier decisions by layer-wise relevance propagation," *PLoS One*, vol. 10, no. 7, p. e0130140, 2015. **1, 3**
- [17] M. Sundararajan, A. Taly, and Q. Yan, "Axiomatic attribution for deep networks," in *ICML*, 2017, pp. 3319–3328. **1, 3, 9, 10, 11, 12, 13, 18**
- [18] R. R. Selvaraju, M. Cogswell, A. Das, R. Vedantam, D. Parikh, and D. Batra, "Grad-CAM: Visual explanations from deep networks via gradient-based localization," *International Journal of Computer Vision*, vol. 128, no. 2, pp. 336–359, 2020. **1, 3, 11, 12**
- [19] S. Khorram, T. Lawson, and L. Fuxin, "iGOS++: integrated gradient optimized saliency by bilateral perturbations," in *CHIL*, 2021, pp. 174–182. **1, 3, 10, 11**
- [20] C. Zhao, K. Wang, X. Zeng, R. Zhao, and A. B. Chan, "Gradient-based visual explanation for transformer-based clip," in *ICML*, 2024, pp. 61 072–61 091. **1, 3, 9, 10, 12, 13**
- [21] S. M. Lundberg and S.-I. Lee, "A unified approach to interpreting model predictions," in *NeurIPS*, 2017, pp. 4765–4774. **1, 3, 10, 11, 12, 13, 14**
- [22] A. Sun, P. Ma, Y. Yuan, and S. Wang, "Explain any concept: Segment anything meets concept-based explanation," in *NeurIPS*, 2023. **1, 3, 10, 11, 12, 13**
- [23] V. Petsiuk, A. Das, and K. Saenko, "RISE: Randomized input sampling for explanation of black-box models," in *BMVC*, 2018, p. 151. **1, 3, 5, 9, 10, 11, 12, 13, 14, 19, 21**
- [24] L. Chen, S. Lou, B. Huang, and Q. Zhang, "Defining and extracting generalizable interaction primitives from dnns," in *ICLR*, 2024. **1, 6, 7**
- [25] D. Liu, H. Deng, X. Cheng, Q. Ren, K. Wang, and Q. Zhang, "Towards the difficulty for a deep neural network to learn concepts of different complexities," in *NeurIPS*, 2023, pp. 41 283–41 304. **1**
- [26] S. Fujishige, *Submodular functions and optimization*. Elsevier, 2005. **1, 4, 6**
- [27] A. Radford, J. W. Kim, C. Hallacy, A. Ramesh, G. Goh, S. Agarwal, G. Sastry, A. Askell, P. Mishkin, J. Clark *et al.*, "Learning transferable visual models from natural language supervision," in *ICML*, 2021, pp. 8748–8763. **2, 8, 9, 10, 11, 12, 19**
- [28] R. Girdhar, A. El-Nouby, Z. Liu, M. Singh, K. V. Alwala, A. Joulin, and I. Misra, "ImageBind: One embedding space to bind them all," in *CVPR*, 2023, pp. 15 180–15 190. **2, 8, 9, 10, 12, 13, 19**
- [29] B. Zhu, B. Lin, M. Ning, Y. Yan, J. Cui, W. HongFa, Y. Pang, W. Jiang, J. Zhang, Z. Li *et al.*, "LanguageBind: Extending video-language pre-training to n-modality by language-based semantic alignment," in *ICLR*, 2024. **2, 8, 9, 10, 12, 13, 19**
- [30] W. Ikezogwo, S. Seyfioglu, F. Ghezloo, D. Geva, F. Sheikh Mohammed, P. K. Anand, R. Krishna, and L. Shapiro, "Quilt-1M: One million image-text pairs for histopathology," in *NeurIPS*, 2024, pp. 37 995–38 017. **2, 8, 13**
- [31] J. Deng, W. Dong, R. Socher, L.-J. Li, K. Li, and L. Fei-Fei, "ImageNet: A large-scale hierarchical image database," in *CVPR*, 2009, pp. 248–255. **2, 8, 12**
- [32] H. Chen, W. Xie, A. Vedaldi, and A. Zisserman, "VGGSound: A large-scale audio-visual dataset," in *ICASSP*, 2020, pp. 721–725. **2, 8, 12**
- [33] P. Welinder, S. Branson, T. Mita, C. Wah, F. Schroff, S. Be-longie, and P. Perona, "Caltech-UCSD Birds 200. Technical Report CNS-TR-2010–001," Technical Report CNS-TR-2010–001, California Institute of Technology, 2010. 1, Tech. Rep., 2010. **2, 8, 12, 14**
- [34] Z. Liu, P. Luo, X. Wang, and X. Tang, "Deep learning face attributes in the wild," in *ICCV*, 2015, pp. 3730–3738. **2, 8**
- [35] Q. Cao, L. Shen, W. Xie, O. M. Parkhi, and A. Zisserman, "VGGFace2: A dataset for recognising faces across pose and age," in *IEEE International Conference on Automatic Face and Gesture Recognition (FG)*, 2018, pp. 67–74. **2, 8**
- [36] A. A. Borkowski, M. M. Bui, L. B. Thomas, C. P. Wilson, L. A. DeLand, and S. M. Mastorides, "Lung and colon cancer histopathological image dataset (LC25000)," *arXiv preprint arXiv:1912.12142*, 2019. **2, 8, 12**
- [37] K. Simonyan, A. Vedaldi, and A. Zisserman, "Deep inside convolutional networks: visualising image classification models and saliency maps," in *ICLR (Workshop Poster)*, 2014. **3, 10, 11, 12**
- [38] L. Chen, S. Lou, B. Huang, and Q. Zhang, "Defining and extracting generalizable interaction primitives from dnns," in *ICLR*, 2024. **3**
- [39] A. Chattopadhyay, A. Sarkar, P. Howlader, and V. N. Balasubramanian, "Grad-CAM++: Generalized gradient-based visual explanations for deep convolutional networks," in *WACV*, 2018, pp. 839–847. **3, 14, 23**
- [40] H. Wang, Z. Wang, M. Du, F. Yang, Z. Zhang, S. Ding, P. Mardziel, and X. Hu, "Score-CAM: Score-weighted visual explanations for convolutional neural networks," in *CVPR Workshops*, 2020, pp. 24–25. **3, 14**
- [41] W. Xie, X.-H. Li, C. C. Cao, and N. L. Zhang, "ViT-CX: causal explanation of vision transformers," in *IJCAI*, 2023, pp. 1569–1577. **3, 10, 12, 13**
- [42] L. S. Shapley, "A value for n-person games," *Annals of Mathematics Studies*, vol. 28, pp. 307–318, 1953. **3**
- [43] L. Chen, S. Lou, K. Zhang, J. Huang, and Q. Zhang, "Harsanyinet: Computing accurate shapley values in a single forward propagation," in *ICML*, 2023, pp. 4804–4825. **3**
- [44] I. E. Kumar, S. Venkatasubramanian, C. Scheidegger, and S. Friedler, "Problems with shapley-value-based explanations as feature importance measures," in *ICML*, 2020, pp. 5491–5500. **3, 7**
- [45] M. T. Ribeiro, S. Singh, and C. Guestrin, "'why should i trust you?' explaining the predictions of any classifier," in *SIGKDD*, 2016, pp. 1135–1144. **3, 11, 12**
- [46] V. Shitole, F. Li, M. Kahng, P. Tadepalli, and A. Fern, "One explanation is not enough: structured attention graphs for image classification," in *NeurIPS*, 2021, pp. 11 352–11 363. **3**
- [47] H. Chefer, S. Gur, and L. Wolf, "Transformer interpretability beyond attention visualization," in *CVPR*, 2021, pp. 782–791. **3**
- [48] T. Darcet, M. Oquab, J. Mairal, and P. Bojanowski, "Vision transformers need registers," in *ICLR*, 2024. **3**
- [49] Y. Gandelsman, A. A. Efros, and J. Steinhardt, "Interpreting clip's image representation via text-based decomposition," in *ICLR*, 2024. **3**
- [50] S. Wu, M. Yuksekgonul, L. Zhang, and J. Zou, "Discover and cure: Concept-aware mitigation of spurious correlation," in *ICML*, 2023, pp. 37 765–37 786. **4**
- [51] A. Abid, M. Yuksekgonul, and J. Zou, "Meaningfully debugging model mistakes using conceptual counterfactual explanations," in *ICML*, 2022, pp. 66–88. **4**
- [52] V. V. Ramaswamy, S. S. Kim, R. Fong, and O. Russakovsky, "Overlooked factors in concept-based explanations: Dataset choice, concept learnability, and human capability," in *CVPR*, 2023, pp. 10 932–10 941. **4**
- [53] S. Kothawade, S. Ghosh, S. Shekhar, Y. Xiang, and R. Iyer, "Talisman: targeted active learning for object detection with rare classes and slices using submodular mutual information," in *ECCV*, 2022, pp. 1–16. **4**
- [54] Y. He, R. Cheng, G. Balasubramanian, Y.-H. H. Tsai, and H. Zhao, "Efficient modality selection in multimodal learning," *Journal of Machine Learning Research*, vol. 25, no. 47, pp. 1–39, 2024. **4**

- [55] A. Catav, B. Fu, Y. Zoabi, A. L. W. Meilik, N. Shomron, J. Ernst, S. Sankararaman, and R. Gilad-Bachrach, "Marginal contribution feature importance—an axiomatic approach for explaining data," in *ICML*, 2021, pp. 1324–1335. [4](#)
- [56] E. Elenberg, A. G. Dimakis, M. Feldman, and A. Karbasi, "Streaming weak submodularity: Interpreting neural networks on the fly," in *NeurIPS*, 2017, pp. 4044–4054. [4](#)
- [57] J. Chen, L. Song, M. Wainwright, and M. Jordan, "Learning to explain: An information-theoretic perspective on model interpretation," in *ICML*, 2018, pp. 883–892. [4](#)
- [58] A. Pervez, P. Lippe, and E. Gavves, "Scalable subset sampling with neural conditional poisson networks," in *ICLR*, 2023, pp. 1–21. [4](#)
- [59] A. Chhabra, P. Li, P. Mohapatra, and H. Liu, "what data benefits my classifier?" enhancing model performance and interpretability through influence-based data selection," in *ICLR*, 2024. [4](#)
- [60] G. L. Nemhauser, L. A. Wolsey, and M. L. Fisher, "An analysis of approximations for maximizing submodular set functions—i," *Mathematical programming*, vol. 14, pp. 265–294, 1978. [4](#)
- [61] B. Mirzasoleiman, A. Badanidiyuru, A. Karbasi, J. Vondrák, and A. Krause, "Lazier than lazy greedy," in *AAAI*, 2015, pp. 1812–1818. [4](#), [6](#), [19](#)
- [62] K. Joseph, K. Singh, and V. N. Balasubramanian, "Submodular batch selection for training deep neural networks," in *IJCAI*, 2019, pp. 2677–2683. [4](#)
- [63] J. Edmonds, "Submodular functions, matroids, and certain polyhedra," *Combinatorial Structures and Their Applications*, pp. 69–87, 1970. [4](#)
- [64] R. Achanta, A. Shaji, K. Smith, A. Lucchi, P. Fua, and S. Süsstrunk, "SLIC superpixels compared to state-of-the-art superpixel methods," *IEEE Transactions on Pattern Analysis and Machine Intelligence*, vol. 34, no. 11, pp. 2274–2282, 2012. [5](#), [8](#)
- [65] A. Kirillov, E. Mintun, N. Ravi, H. Mao, C. Rolland, L. Gustafson, T. Xiao, S. Whitehead, A. C. Berg, W.-Y. Lo, P. Dollar, and R. Girshick, "Segment anything," in *ICCV*, 2023, pp. 4015–4026. [5](#), [8](#), [12](#), [23](#)
- [66] M. Noroozi and P. Favaro, "Unsupervised learning of visual representations by solving jigsaw puzzles," in *ECCV*, 2016, pp. 69–84. [5](#)
- [67] X. Guo, C. Yang, Y. Liu, and Y. Yuan, "Learn to threshold: Thresholdnet with confidence-guided manifold mixup for polyp segmentation," *IEEE Transactions on Medical Imaging*, vol. 40, no. 4, pp. 1134–1146, 2020. [5](#)
- [68] M. Shu, W. Nie, D.-A. Huang, Z. Yu, T. Goldstein, A. Anandkumar, and C. Xiao, "Test-time prompt tuning for zero-shot generalization in vision-language models," in *NeurIPS*, 2022, pp. 14 274–14 289. [5](#)
- [69] X. Guo, J. Liu, T. Liu, and Y. Yuan, "Handling open-set noise and novel target recognition in domain adaptive semantic segmentation," *IEEE Transactions on Pattern Analysis and Machine Intelligence*, vol. 45, no. 8, pp. 9846–9861, 2023. [5](#)
- [70] H. Wang, Y. Wang, Z. Zhou, X. Ji, D. Gong, J. Zhou, Z. Li, and W. Liu, "Cosface: Large margin cosine loss for deep face recognition," in *CVPR*, 2018, pp. 5265–5274. [6](#)
- [71] J. Deng, J. Guo, N. Xue, and S. Zafeiriou, "Arcface: Additive angular margin loss for deep face recognition," in *CVPR*, 2019, pp. 4690–4699. [6](#), [8](#)
- [72] K. Wei, R. Iyer, and J. Bilmes, "Submodularity in data subset selection and active learning," in *ICML*, 2015, pp. 1954–1963. [6](#)
- [73] K. He, X. Zhang, S. Ren, and J. Sun, "Deep residual learning for image recognition," in *CVPR*, 2016, pp. 770–778. [8](#), [10](#), [11](#), [14](#), [19](#)
- [74] A. Dosovitskiy, L. Beyer, A. Kolesnikov, D. Weissenborn, X. Zhai, T. Unterthiner, M. Dehghani, M. Minderer, G. Heigold, S. Gelly *et al.*, "An image is worth 16x16 words: Transformers for image recognition at scale," in *ICLR*, 2021. [8](#), [11](#)
- [75] Z. Liu, Y. Lin, Y. Cao, H. Hu, Y. Wei, Z. Zhang, S. Lin, and B. Guo, "Swin transformer: Hierarchical vision transformer using shifted windows," in *ICCV*, 2021, pp. 10012–10 022. [8](#), [11](#), [19](#)
- [76] L. Zhu, B. Liao, Q. Zhang, X. Wang, W. Liu, and X. Wang, "Vision mamba: Efficient visual representation learning with bidirectional state space model," in *ICML*, 2024. [8](#), [11](#), [19](#)
- [77] A. Hatamizadeh and J. Kautz, "MambaVision: A hybrid mamba-transformer vision backbone," *arXiv preprint arXiv:2407.08083*, 2024. [8](#), [11](#), [19](#)
- [78] M. Sandler, A. Howard, M. Zhu, A. Zhmoginov, and L.-C. Chen, "MobileNetV2: Inverted residuals and linear bottlenecks," in *CVPR*, 2018, pp. 4510–4520. [8](#), [14](#)
- [79] M. Tan and Q. Le, "EfficientNetV2: Smaller models and faster training," in *ICML*, 2021, pp. 10 096–10 106. [8](#), [14](#)
- [80] U. Bhatt, A. Weller, and J. M. Moura, "Evaluating and aggregating feature-based model explanations," in *IJCAI*, 2021, pp. 3016–3022. [9](#)
- [81] J. Li, K. Kuang, L. Li, L. Chen, S. Zhang, J. Shao, and J. Xiao, "Instance-wise or class-wise? a tale of neighbor shapley for concept-based explanation," in *ACM MM*, 2021, pp. 3664–3672. [9](#)
- [82] Y. Ma, A. Øland, A. Ragni, B. M. Del Sette, C. Saitis, C. Donahue, C. Lin, C. Plachouras, E. Benetos, E. Quinton *et al.*, "Foundation models for music: A survey," *arXiv preprint arXiv:2408.14340*, 2024. [12](#)
- [83] S. Hooker, D. Erhan, P.-J. Kindermans, and B. Kim, "A benchmark for interpretability methods in deep neural networks," in *NeurIPS*, 2019, pp. 9734–9745. [12](#)
- [84] A. Shrikumar, P. Greenside, A. Shcherbina, and A. Kundaje, "Not just a black box: Learning important features through propagating activation differences," *arXiv preprint arXiv:1605.01713*, 2016. [12](#)
- [85] D. Smilkov, N. Thorat, B. Kim, F. Viégas, and M. Wattenberg, "SmoothGrad: removing noise by adding noise," *arXiv preprint arXiv:1706.03825*, 2017. [12](#)
- [86] J. Seo, J. Choe, J. Koo, S. Jeon, B. Kim, and T. Jeon, "Noise-adding methods of saliency map as series of higher order partial derivative," *arXiv preprint arXiv:1806.03000*, 2018. [12](#)
- [87] M. Ancona, E. Ceolini, C. Öztireli, and M. Gross, "Towards better understanding of gradient-based attribution methods for deep neural networks," in *ICLR*, 2018. [12](#)
- [88] T. Fel, R. Cadène, M. Chalvidal, M. Cord, D. Vigouroux, and T. Serre, "Look at the variance! efficient black-box explanations with sobol-based sensitivity analysis," in *NeurIPS*, 2021, pp. 26 005–26 014. [12](#)
- [89] G. Montavon, S. Lapuschkin, A. Binder, W. Samek, and K.-R. Müller, "Explaining nonlinear classification decisions with deep taylor decomposition," *Pattern recognition*, vol. 65, pp. 211–222, 2017. [18](#)



Ruoyu Chen is currently working toward the Ph.D. degree in the School of Cyber Security, University of Chinese Academy of Sciences, China. He received his B.E. degree in measurement & control technology and instrument from Northeastern University, China in 2021. He has published multiple top journals and conference papers, such as ICLR. He has served as a reviewer for several top journals and conferences such as T-PAMI, ECCV, CVPR, ICML, ICCV, ICLR, and NeurIPS. His research interests mainly include computer vision and interpretable AI.



Siyuan Liang is a Research Fellow at the School of Computing, National University of Singapore, specializing in adversarial machine learning and computer vision. She obtained her Ph.D. in Cyberspace Security from the University of the Chinese Academy of Sciences and a Bachelor's degree in Software Engineering from Sichuan University. Her work primarily focuses on developing robust AI models to enhance computer vision security.



Jingzhi Li is currently an associate professor with the Institute of Information Engineering, Chinese Academy of Sciences, Beijing, China. She received the Ph.D. degree in cyberspace security from the University of Chinese Academy of Sciences, Beijing, China. Her current research interests include image processing, face recognition security, and multimedia privacy.



Shiming Liu is a Senior Research Scientist at Huawei Technologies Co., Ltd., China. He received the Ph.D. degree in intelligent manufacturing from the Department of Mechanical Engineering, Imperial College London, UK, in 2022. His current research interests include advanced safety-guard for autonomous driving system (ADS), SOTIF, AI interpretability and AI failure detection.



Li Liu (Senior Member, IEEE) received the Ph.D. degree in information and communication engineering from the National University of Defense Technology (NUDT), China, in 2012. She is currently a Full Professor with the College of System Engineering, National University of Defense Technology. During her Ph.D. study, she spent more than two years as a Visiting Student at the University of Waterloo, Canada, from 2008 to 2010. From 2015 to 2016, she

spent ten months visiting the Multimedia Laboratory at the Chinese University of Hong Kong. From 2016.12 to 2018.11, she worked as a senior researcher at the Machine Vision Group at the University of Oulu, Finland. Her current research interests include Computer Vision, Machine Learning, Artificial Intelligence, Trustworthy AI, and Synthetic Aperture Radar. Her papers have currently over 18,000+ citations in Google Scholar.



Hua Zhang is a Professor with the Institute of Information Engineering, Chinese Academy of Sciences. He received the Ph.D. degree in computer science from the School of Computer Science and Technology, Tianjin University, Tianjin, China in 2015. His research interests include computer vision, multimedia, and machine learning.



Xiaochun Cao (Senior Member, IEEE) is a Professor and Dean of the School of Cyber Science and Technology, Shenzhen Campus of Sun Yat-sen University. He received the B.E. and M.E. degrees both in computer science from Beihang University (BUAA), China, and the Ph.D. degree in computer science from the University of Central Florida, USA, with his dissertation nominated for the university level Outstanding Dissertation Award. After graduation, he

spent about three years at ObjectVideo Inc. as a Research Scientist. From 2008 to 2012, he was a professor at Tianjin University. Before joining SYSU, he was a professor at the Institute of Information Engineering, Chinese Academy of Sciences. He has authored and co-authored over 200 journal and conference papers. In 2004 and 2010, he was the recipients of the Piero Zamperoni best student paper award at the International Conference on Pattern Recognition. He is on the editorial boards of IEEE TRANSACTIONS ON PATTERN ANALYSIS AND MACHINE INTELLIGENCE and IEEE TRANSACTIONS ON IMAGE PROCESSING, and was on the editorial boards of IEEE TRANSACTIONS ON CIRCUITS AND SYSTEMS FOR VIDEO TECHNOLOGY and IEEE TRANSACTIONS ON MULTIMEDIA.

APPENDIX A THEORY PROOF

A.1 Proof of Lemma 1 (Diminishing returns)

Proof. Consider two sub-sets S_a and S_b in set V , where $S_a \subseteq S_b \subseteq V$. Given an element α , where $\alpha = V \setminus S_b$. The necessary and sufficient conditions for the function $\mathcal{F}(\cdot)$ to satisfy the submodular property are:

$$\mathcal{F}(S_a \cup \{\alpha\}) - \mathcal{F}(S_a) \geq \mathcal{F}(S_b \cup \{\alpha\}) - \mathcal{F}(S_b). \quad (16)$$

For Eq. 3, let $G(S_a) = F(S_a) \circ \mathbf{f}_s$. Assuming that the individual element α of the collection division is relatively small, according to the Taylor decomposition [89], we can locally approximate $G(S_a + \alpha) = G(S_a) + \nabla G(S_a) \cdot \alpha$. Assuming that the searched α is valid, i.e., $\nabla G(S_a) > 0$. Thus:

$$\begin{aligned} & s_{\text{cons.}}(S_a + \alpha, \mathbf{f}_s) - s_{\text{cons.}}(S_a, \mathbf{f}_s) \\ &= \frac{G(S_a) + \nabla G(S_a) \cdot \alpha}{\|F(S_a) + \nabla F(S_a) \cdot \alpha\|} - \frac{G(S_a)}{\|F(S_a)\|} \\ &\simeq \frac{\nabla G(S_a) \cdot \alpha}{\|F(S_a)\|}, \end{aligned} \quad (17)$$

since $\nabla G(S_a) > 0$ and α is valid, mean that $\nabla G(S_a) \cdot \alpha$ has a very high probability of having a positive impact on the explainability. Furthermore, $S_a \cap \alpha = \emptyset$, S_a and α do not overlap in the image space, and α is small. Therefore, even when the $\nabla G(S_a)$ and α directions are not consistent, $\nabla G(S_a) \cdot \alpha$ is small. If both S_a and S_b contain positive subsets, then $\nabla G(S_b)$ will become less severe or even disappear [17]. Otherwise, it means that the remaining α can no longer produce interpretable results, i.e., $\nabla G(S_a) \cdot \alpha \approx 0$. Then, we have:

$$\begin{aligned} & s_{\text{cons.}}(S_a + \alpha, \mathbf{f}_s) - s_{\text{cons.}}(S_a, \mathbf{f}_s) \\ & - (s_{\text{cons.}}(S_b + \alpha, \mathbf{f}_s) - s_{\text{cons.}}(S_b, \mathbf{f}_s)) > 0^-. \end{aligned} \quad (18)$$

For Eq. 4, let $G(\mathbf{I} - S_a) = F(\mathbf{I} - S_a) \circ \mathbf{f}_s$. Assuming that the individual element α of the collection division is relatively small, according to the Taylor decomposition, we can locally approximate $G(\mathbf{I} - S_a - \alpha) = G(\mathbf{I} - S_a) - \nabla G(\mathbf{I} - S_a) \cdot \alpha$. Assuming that the searched alpha is valid, i.e., $\nabla G(\mathbf{I} - S_a) > 0$. Thus:

$$\begin{aligned} & s_{\text{colla.}}(S_a + \alpha, \mathbf{I}, \mathbf{f}_s) - s_{\text{colla.}}(S_a, \mathbf{I}, \mathbf{f}_s) \\ &= \frac{G(\mathbf{I} - S_a)}{\|F(\mathbf{I} - S_a)\|} - \frac{G(\mathbf{I} - S_a) - \nabla G(\mathbf{I} - S_a) \cdot \alpha}{\|F(\mathbf{I} - S_a - \alpha)\|} \\ &\simeq \frac{\nabla G(\mathbf{I} - S_a) \cdot \alpha}{\|F(\mathbf{I} - S_a)\|}, \end{aligned} \quad (19)$$

likewise, since $\nabla G(\mathbf{I} - S_a) > 0$ and α is valid, means that $\nabla G(\mathbf{I} - S_a) \cdot \alpha$ has a very high probability of having a positive impact on the explainability. If both S_a and S_b contain positive subsets, then $\nabla G(\mathbf{I} - S_b)$ will become less severe or even disappear. Otherwise, it means that the remaining α can no longer produce interpretable results, i.e., $\nabla G(\mathbf{I} - S_a) \cdot \alpha \approx 0$. Then, we have:

$$\begin{aligned} & s_{\text{colla.}}(S_a + \alpha, \mathbf{I}, \mathbf{f}_s) - s_{\text{colla.}}(S_a, \mathbf{I}, \mathbf{f}_s) \\ & - (s_{\text{colla.}}(S_b + \alpha, \mathbf{I}, \mathbf{f}_s) - s_{\text{colla.}}(S_b, \mathbf{I}, \mathbf{f}_s)) > 0^-. \end{aligned} \quad (20)$$

For Eq. 5, assuming that the individual element α of the collection division is relatively small, according to the Taylor decomposition, we can locally approximate $G_c(S_a) = P(y_c | S_a) = F(S_a) \circ \mathbf{f}_{s,c}$. Thus:

$$\begin{aligned} & s_{\text{conf.}}(S_a + \alpha) - s_{\text{conf.}}(S_a) \\ &= \frac{\sum_{i=1}^C (G_i(S_a) + \nabla G_i(S_a) \cdot \alpha) \log(G_i(S_a) + \nabla G_i(S_a) \cdot \alpha)}{\log(C)} \\ & \quad - \frac{\sum_{i=1}^C G_i(S_a) \log(G_i(S_a))}{\log(C)} \\ &\simeq \frac{\sum_{i=1}^C G_i(S_a) \log \frac{G_i(S_a) + \nabla G_i(S_a) \cdot \alpha}{G_i(S_a)}}{\log(C)}, \end{aligned} \quad (21)$$

let c denote the ground truth class, since $S_a \cap \alpha = \emptyset$, S_a and α do not overlap in the image space, and α is small, $\nabla G(S_a) \cdot \alpha$ is small, that we have:

$$\begin{aligned} & G_c(S_a) \log \left(1 + \frac{\nabla G_c(S_a) \cdot \alpha}{G_c(S_a)} \right) \\ & - G_c(S_b) \log \left(1 + \frac{\nabla G_c(S_b) \cdot \alpha}{G_c(S_b)} \right) \approx 0, \end{aligned} \quad (22)$$

where for terms not of belong to class c , $G_c(S_a)$ and $G_i(S_a) + \nabla G_i(S_a) \cdot \alpha$ tend to 0, so we have:

$$s_{\text{conf.}}(S_a + \alpha) - s_{\text{conf.}}(S_a) - (s_{\text{conf.}}(S_b + \alpha) - s_{\text{conf.}}(S_b)) \approx 0. \quad (23)$$

For Eq. 7, when a new element α is added to the set S_a , the minimum distance between elements in S_a and other elements may be further reduced, i.e., for any element $s_i \in S_a$, we have $\min_{s_j \in S_a \cup \{\alpha\}, s_j \neq s_i} \text{dist}(F(s_i), F(s_j)) \leq \min_{s_j \in S_a, s_j \neq s_i} \text{dist}(F(s_i), F(s_j))$. Thus:

$$\begin{aligned} s_{\text{eff.}}(S_a \cup \{\alpha\}) &= \min_{s_i \in S_a} \text{dist}(F(\alpha), F(s_i)) \\ &+ \sum_{s_j \in S_a} \min_{s_i \in S_a \cup \{\alpha\}, s_i \neq s_j} \text{dist}(F(s_i), F(s_j)) \\ &= \min_{s_i \in S_a} \text{dist}(F(\alpha), F(s_i)) \\ &+ \sum_{s_i \in S_a} \min_{s_j \in S_a, s_j \neq s_i} \text{dist}(F(s_i), F(s_j)) \\ &- \varepsilon_a, \end{aligned} \quad (24)$$

where ε_a is a constant, which is the sum of the minimum distance reductions of the elements in the original S_a after α is added. Then, we have:

$$s_{\text{eff.}}(S_a \cup \{\alpha\}) - s_{\text{eff.}}(S_a) = \min_{s_i \in S_a} \text{dist}(F(\alpha), F(s_i)) - \varepsilon_a, \quad (25)$$

and in the same way,

$$s_{\text{eff.}}(S_b \cup \{\alpha\}) - s_{\text{eff.}}(S_b) = \min_{s_i \in S_b} \text{dist}(F(\alpha), F(s_i)) - \varepsilon_b, \quad (26)$$

since $S_a \subseteq S_b$, the minimum distance between alpha and elements in $S_b \setminus S_a$ may be smaller than the minimum distance between alpha and elements in S_a , thus,

$$\min_{s_i \in S_a} \text{dist}(F(\alpha), F(s_i)) \geq \min_{s_i \in S_b} \text{dist}(F(\alpha), F(s_i)),$$

since there are more elements in S_b than in S_a , more elements in S_b have the shortest distance from α , that, $\varepsilon_b \geq \varepsilon_a$. Therefore, we have:

$$s_{\text{eff.}}(S_a \cup \{\alpha\}) - s_{\text{eff.}}(S_a) \geq s_{\text{eff.}}(S_b \cup \{\alpha\}) - s_{\text{eff.}}(S_b). \quad (27)$$

Combining Eq.18, 20, 23, and 27 we can get:

$$\mathcal{F}(S_a \cup \{\alpha\}) - \mathcal{F}(S_a) \geq \mathcal{F}(S_b \cup \{\alpha\}) - \mathcal{F}(S_b), \quad (28)$$

hence, we can prove that Eq. 8 is a submodular function. \square

A.2 Proof of Lemma 2 (Monotonically non-decreasing)

Proof. Consider a subset S , given an element α , assuming that α is contributing to interpretation. The necessary and sufficient conditions for the function $\mathcal{F}(\cdot)$ to satisfy the property of monotonically non-decreasing is:

$$\mathcal{F}(S \cup \{\alpha\}) - \mathcal{F}(S) > 0, \quad (29)$$

where, for Eq. 3, assuming that the searched α is valid,

$$s_{\text{cons.}}(S + \alpha, \mathbf{f}_s) - s_{\text{cons.}}(S, \mathbf{f}_s) \simeq \frac{\nabla G(S) \cdot \alpha}{\|F(S)\|} > 0, \quad (30)$$

likewise, for Eq. 4,

$$\begin{aligned} &s_{\text{colla.}}(S + \alpha, \mathbf{I}, \mathbf{f}_s) - s_{\text{colla.}}(S, \mathbf{I}, \mathbf{f}_s) \\ &\simeq \frac{\nabla G(\mathbf{I} - S) \cdot \alpha}{\|F(\mathbf{I} - S)\|} > 0. \end{aligned} \quad (31)$$

For Eq. 5:

$$\begin{aligned} &s_{\text{conf.}}(S + \alpha) - s_{\text{conf.}}(S) \\ &\simeq \frac{\sum_{i=1}^C G_i(S) \log \frac{G_i(S) + \nabla G_i(S) \cdot \alpha}{G_i(S)}}{\log(C)}, \end{aligned} \quad (32)$$

since α is contributing to interpretation, for the ground truth class c , $\nabla G_c(S) > 0$, and $\nabla G_c(S) > 0$; where for the term not belong to c , $G_i(S) \approx 0$, thus:

$$s_{\text{conf.}}(S + \alpha) - s_{\text{conf.}}(S) > 0. \quad (33)$$

For Eq. 7,

$$s_{\text{eff.}}(S \cup \{\alpha\}) - s_{\text{eff.}}(S) = \min_{s_i \in S} \text{dist}(F(\alpha), F(s_i)) - \varepsilon,$$

since effective element α are selected as much as possible, the value ε will be small,

$$s_{\text{eff.}}(S \cup \{\alpha\}) - s_{\text{eff.}}(S) \simeq \min_{s_i \in S} \text{dist}(F(\alpha), F(s_i)) > 0. \quad (34)$$

Combining Eq. 30, 31, 33, and 34 we can get:

$$\mathcal{F}(S \cup \{\alpha\}) - \mathcal{F}(S) > 0, \quad (35)$$

hence, we can prove that Eq. 8 is monotonically non-decreasing. \square

A.3 Proof of Theorem 1 (Bidirectional greedy search optimality bound)

Proof. Suppose the optimal solution is S^* , and $1 - \epsilon$ is the probability that S_d overlaps with S^* . Therefore, based on the reasoning of Mirzasoleiman *et al.* [61], solution S can be obtained, which satisfies the following approximate guarantee:

$$\mathcal{F}(S) \geq \left(1 - \frac{1}{e} - \epsilon\right) \mathcal{F}(S^*), \quad (36)$$

where, ϵ is affected by n_p , because the larger n_p is, the more likely S_p will contain the least important samples, thus not affecting the missing of important samples in $S_d = V \setminus (S_{\text{forward}} \cup S_{\text{reverse}})$. By selecting an appropriate n_p value, we can accelerate the attribution process while maintaining the faithfulness of the attribution graph. \square

APPENDIX B

ADDITIONAL VISUALIZATIONS

In this section, we present more interpretable visualizations of our results and compare them with those from other methods.

B.1 Additional Visualization on Foundation Model

Fig. 11 presents more interpretable attribution results for three multimodal foundation models (CLIP [27], ImageBind [28], and LanguageBind [29]) with ViT backbone on the ImageNet dataset.

Fig. 12 presents interpretable attribution results for CLIP (ResNet-101) [27] on the ImageNet dataset. We compare with RISE [23] and HSIC-Attribution [9] methods, showing the advantages of our method.

B.2 Visualization on ResNet-101

Fig. 13 presents interpretable attribution results for single-modal ResNet-101 [73] on the ImageNet dataset. We compare with RISE [23] and HSIC-Attribution [9] methods, showing the advantages of our method.

B.3 Visualization on Vision Transformer

Fig. 14 presents more interpretable attribution results for single-modal Vision Transformer and Swin Transformer [75] models on the ImageNet dataset. We compare with HSIC-Attribution [9] methods, showing the advantages of our method.

B.4 Visualization on Vision Mamba

Fig. 15 presents more interpretable attribution results for single-modal Vision Mamba (base) [76] and MambaVision (L2) [77] models on the ImageNet dataset. We compare with HSIC-Attribution [9] methods, showing the advantages of our method.

APPENDIX C

VISUALIZATION OF MODEL MISTAKE ON CUB-200-2011

We demonstrate the ability of our method to attribution images that are incorrectly predicted by the model on the CUB-200-2011 dataset. Fig. 16 shows the comparison between our method and HSIC-Attribution [9] and the previous version [8] on ResNet-101 model. It can be found that the current version of the method can have a flatter Insertion curve, which means that the attribution effect is better. In addition, we also show the attribution effects of different models on HSIC-Attribution and our method in Fig. 17. We include the sub-region division strategy based on superpixel segmentation and SAM.

CLIP (ResNet-101)

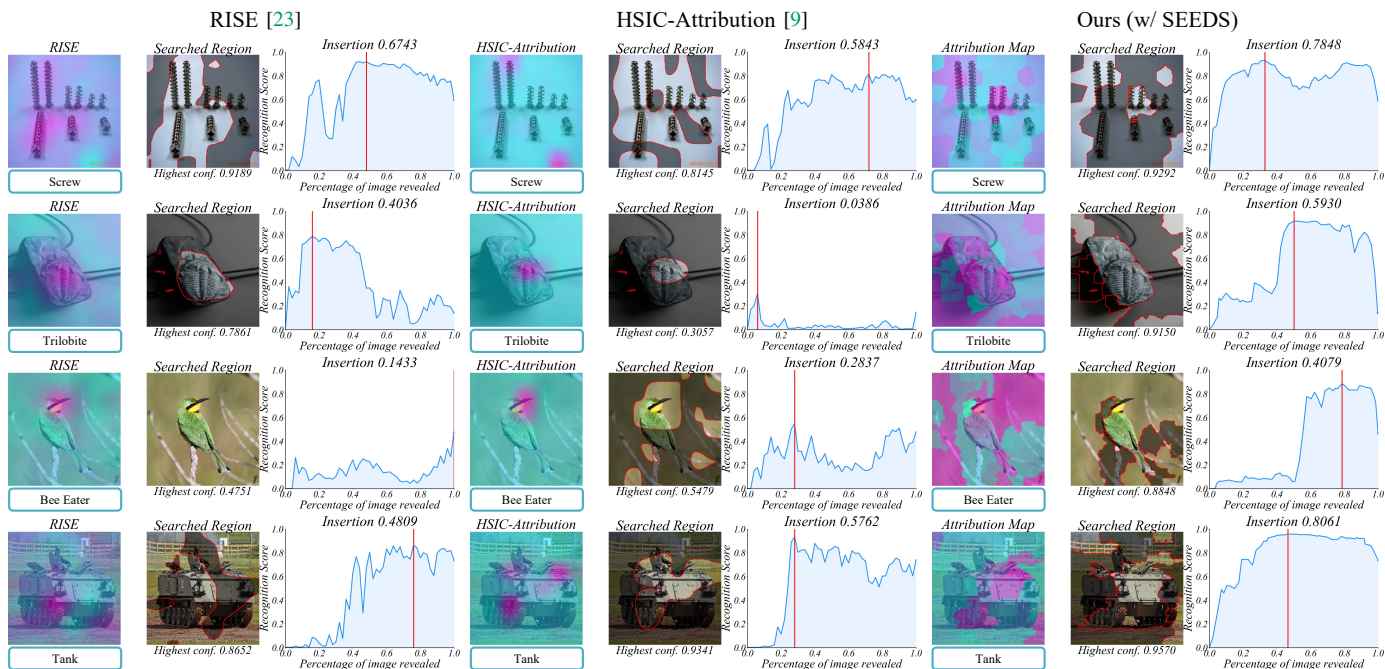


Fig. 12. Additional interpretation visualization for CLIP (ResNet-101) on the ImageNet dataset.

ResNet-101

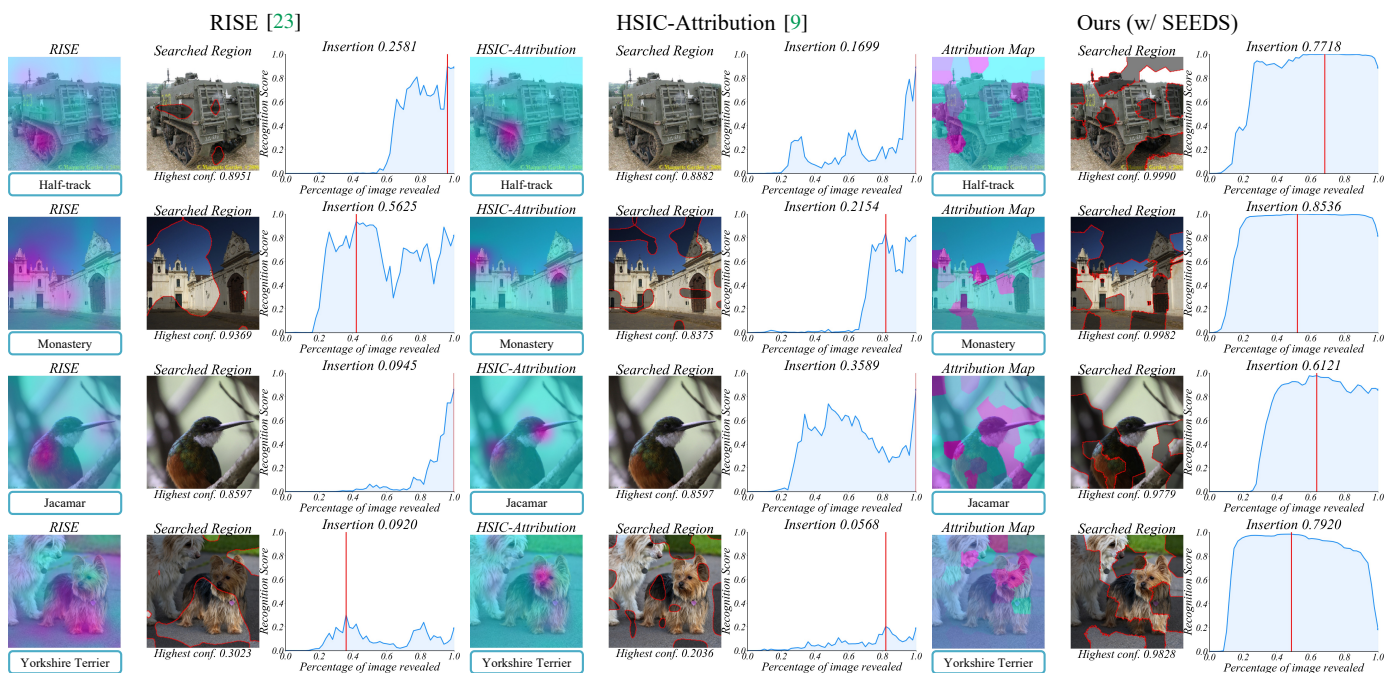


Fig. 13. Additional interpretation visualization for single-modal ResNet-101 on the ImageNet dataset.

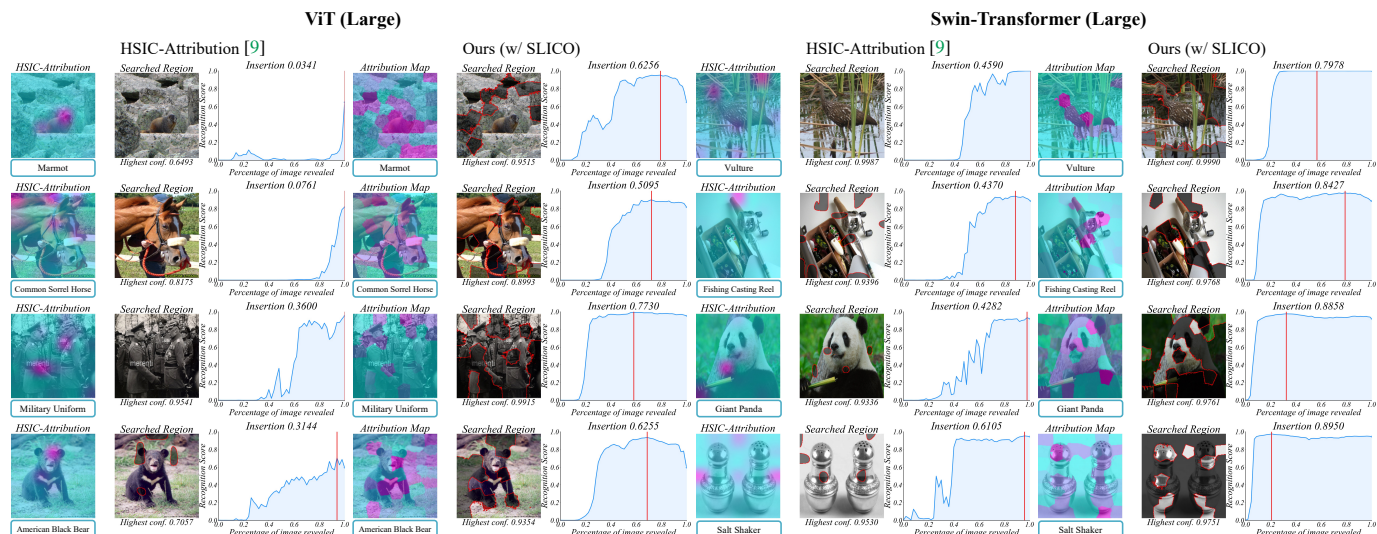


Fig. 14. Additional interpretation visualization for single-modal vision transformer (Large) and swin-transformer (Large) on the ImageNet dataset.

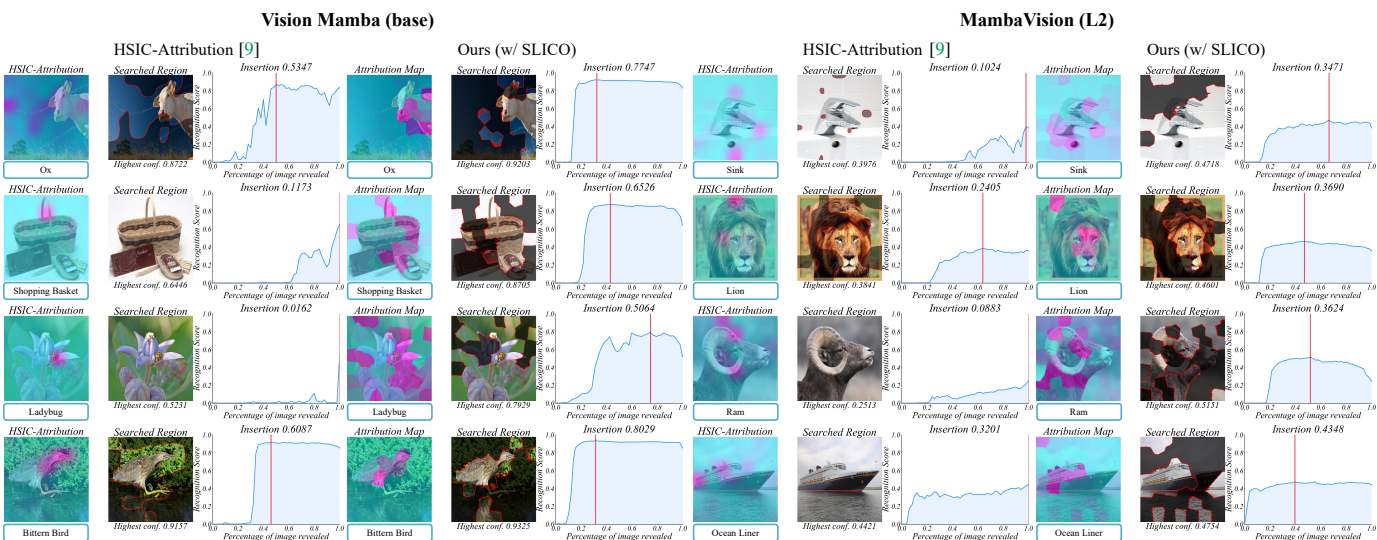
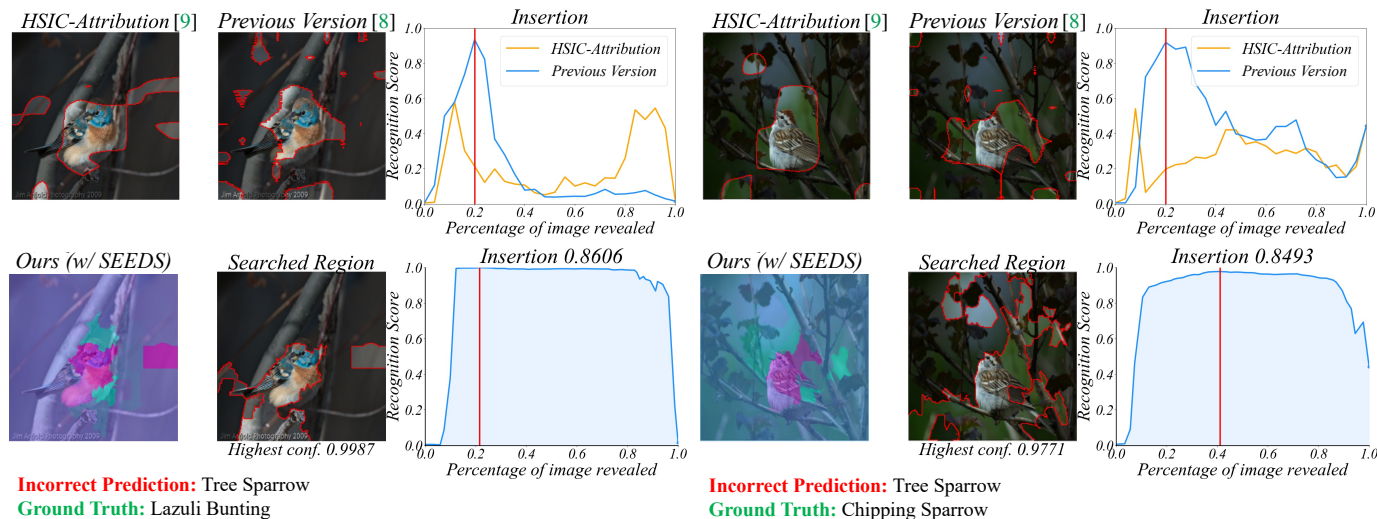


Fig. 15. Additional interpretation visualization for single-modal vision mamba (base) and mambavision (L2) on the ImageNet dataset.



Incorrect Prediction: Tree Sparrow
Ground Truth: Lazuli Bunting

Incorrect Prediction: Tree Sparrow
Ground Truth: Chipping Sparrow

Fig. 16. Visualization of the method for discovering what causes model prediction errors on the CUB-200-2011 dataset. The first row shows the results of the HSIC-Attribution method and the previous version method, and the second row shows the results of the current version method. The Insertion curve shows the correlation between the searched region and ground truth class prediction confidence. The highlighted region matches the searched region indicated by the red line in the curve, and the dark region is the error cause identified by the method.

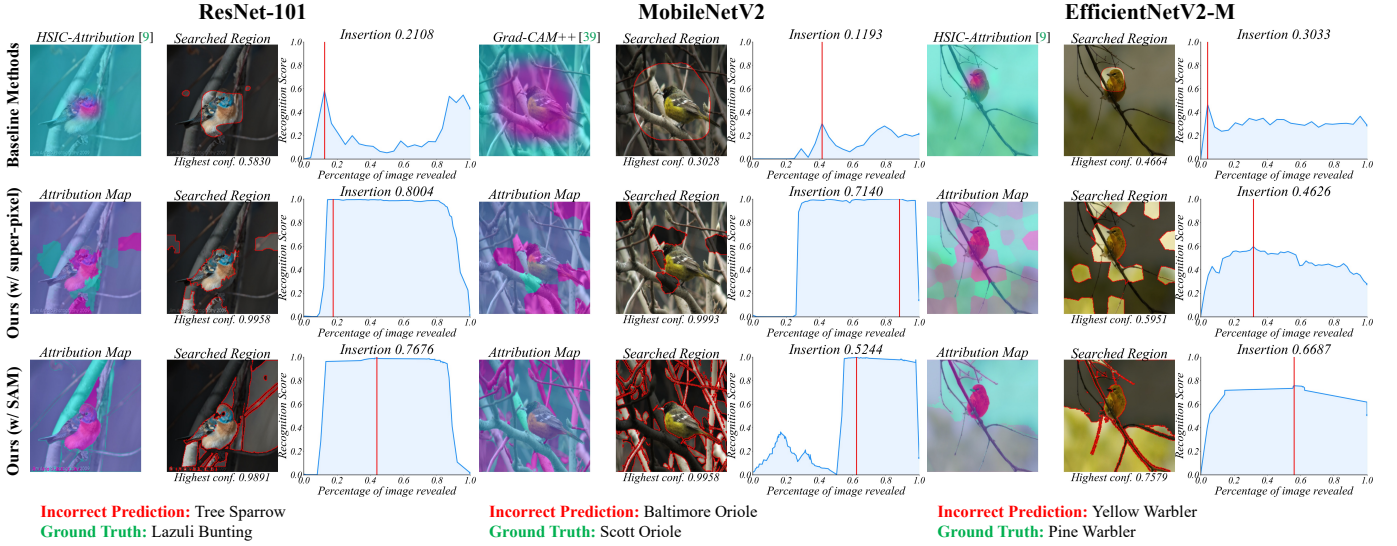


Fig. 17. Visualization of the method for discovering what causes model prediction errors on the CUB-200-2011 dataset. The first row shows the results of the HSIC-Attribution method and the previous version method, and the second row shows the results of the current version method. The Insertion curve shows the correlation between the searched region and ground truth class prediction confidence. The highlighted region matches the searched region indicated by the red line in the curve, and the dark region is the error cause identified by the method.

APPENDIX D

SUB-REGION DIVISION ALGORITHM BASED ON SEGMENT ANYTHING MODEL

Algorithm 2 demonstrates how to use Segment Anything (SAM) [65] for sub-region division. As SAM produces overlapping sub-regions, we further split these overlapping regions to create more fine-grained sub-regions.

Algorithm 2: Sub-region division algorithm based on Segment Anything Model [65]

Input: Image $\mathbf{I} \in \mathbb{R}^{w \times h \times 3}$, Segment Anything Model $\text{SAM}(\cdot)$, delete threshold δ .

Output: An set V .

```

1  $V \leftarrow \emptyset$ ;      /* Initiate the operation of
    sub-region division */
2  $V_M = \text{SAM}(\mathbf{I})$ ;
3 for  $i = 1$  to  $|V_M| - 1$  do
4    for  $j = i + 1$  to  $|V_M|$  do
5      $\mathbf{M}_{\text{inters.}} = V_M[i] \circ V_M[j]$ ;
6     if  $\text{sum}(\mathbf{M}_{\text{inters.}}) \neq 0$  then
7        if  $\text{sum}(V_M[i]) > \text{sum}(V_M[j])$  then
8          $V_M[i] = V_M[i] - \mathbf{M}_{\text{inters.}}$ ;
9        else
10         $V_M[j] = V_M[j] - \mathbf{M}_{\text{inters.}}$ ;
11     end
12 end
13 for  $i = 1$  to  $|V_M|$  do
14    if  $\text{mean}(V_M[i]) > \delta$  then
15      $V \leftarrow V \cup \{V_M[i] \circ \mathbf{I}\}$ ;
16 end
17  $\mathbf{I}_r = \mathbf{I}_r$ ;      /* A region that is not divided
    by  $\text{SAM}(\cdot)$ . */
18 for  $i = 1$  to  $|V_M|$  do
19     $\mathbf{I}_r = \mathbf{I}_r - V_M[i]$ ;
20 end
21  $V \leftarrow V \cup \{\mathbf{I}_r\}$ ;
22 return  $V$ 

```
